We are IntechOpen,
the world's leading publisher of
Open Access books
Built by scientists, for scientists

6,900
Open access books available

186,000
International authors and editors

200M
Downloads

Our authors are among the

154
Countries delivered to

TOP 1%
most cited scientists

12.2%
Contributors from top 500 universities

CLARIVATE ANALYTICS
BOOK CITATION INDEX
INDEXED

WEB OF SCIENCE™

Selection of our books indexed in the Book Citation Index
in Web of Science™ Core Collection (BKCI)

Interested in publishing with us?
Contact book.department@intechopen.com

Epitaxial Integration of Ferroelectric BaTiO$_3$ with Semiconductor Si: From a Structure-Property Correlation Point of View

Liang Qiao and Xiaofang Bi

*Key Laboratory of Aerospace Materials and Performance
(Ministry of Education), School of Materials Science and Engineering,
Beijing University of Aeronautics and Astronautics, Beijing,
People's Republic of China*

1. Introduction

Ferroelectric thin films have attracted significant attention recently, due to their great potential for practical use in microelectronic and optoelectronic applications, such as non-volatile ferroelectric random access memories (NvFRAM), high-density capacitors, micro-electromechanical system (MEMS) and electro-optic devices etc. [1,2]. Among all the ferroelectric materials, BaTiO$_3$ (BTO) is most widely investigated not only for its simple chemical composition and remarkable properties (high dielectric constant and non-linear optical properties) but also because of their lead-free and environmental-friendly characteristic, which has become increasingly important from a long term point of view [3]. To date, a number of preparation techniques such as vacuum evaporation [4], sputtering [5], pulsed laser deposition (PLD) [6], molecular beam epitaxy (MBE) [7], metalorganic chemical vapor deposition (MOCVD) [8], sol-gel [9], and hydrothermal method [10] have been reported to fabricate BTO thin films.

On the other hand, newer device concepts may become realities if ferroelectricity can be coupled with conventional Si semiconductor technology. For example, ferroelectric field effect transistors, in which no power is required to maintain logic states, enter the realm of the possible if high-quality ferroelectric oxides can be grown epitaxially on Si with the right kinds of interfaces [11,12]. The criterion for successful integration with semiconductors is the minimum critical thickness for ferroelectricity, which must be of the order of a few nm in order to be compatible with very large scale integration. When in intimate contact with a semiconductor such that the polarization vector is normal to the interface, a ferroelectric oxide tends to develop a depolarizing field that suppresses the ferroelectric ground state. This depolarizing field can be eliminated if the ferroelectric oxide is sandwiched by metal electrodes which perfectly screen the polarization field. However, if the ferroelectric is in contact with a semiconductor and the interface state density is zero, there is very little screening of the polarization field, and the ferroelectric critical thickness becomes unacceptably large.

Meanwhile, the current request of downscaling needs for microelectronic devices has highlighted the importance of size effects as well as strain and dislocation influence on the

properties of ferroelectric thin films [13-16]. Change of film strain field, either tensile or compressive, will elongate or shorten the corresponding lattice parameter. As a result, film tetragonality, polarization direction, domain configuration as well as dielectric constant along different axis will be subsequently engineered by that change of strain. However, due to large difference of lattice parameters and thermal expansion coefficients (TECs) between BTO and Si, most of the films reported to date are in an in-plane tensile strain state [12]. Although tensile BTO films with in-plane polarization are suitable for electric-optical applications [17], there are many applications in which a compressive strain leading to out-of-plane polarization is desired, e.g. the ferroelectric memory devices and quantum computing architecture [18,19]. An effective approach to control the strain state of BTO films is to choose an appropriate buffer layer by taking lattice constants and TECs into account. For example, Vaithyanathan *et al.* [20] has recently demonstrated that a $Ba_{0.7}Sr_{0.3}TiO_3$ layer of 300 Å enables a BTO film of 100 Å on Si to be in a compressive strain state, which is characterized by a complete *c*-axis orientation.

It is known that the well-developed $LaNiO_3$ (LNO) thin film serves not only as a crystallographic seed layer but also as a conductive layer. What is more, the lattice parameter of LNO has a good match with that of BTO (along [100] direction) and Si (along [110] direction) and the TEC of LNO (8.2×10^{-6} K^{-1}) is in between the values of BTO (10.4×10^{-6} K^{-1}) and Si (1.4×10^{-6} K^{-1}) [21,22]. Therefore, the strain state for the LNO buffer layer is expected to have a great influence on the strain state in its adjacent BTO layer, and a compressive strain in BTO on Si substrate could be induced by controlling the strain state in LNO. In this chapter, we will show that by insertion of a LNO buffer layer, high quality of BTO films can be integrated with Si(001) substrates and the structure-property correlations of BTO is largely dependent on the LNO buffer layer. A transformation from tensile to compressive strain state for BTO can be tuned by thickness of LNO. The corresponding microstructure and phase transition features of the BTO films will also be discussed.

2. Materials and experimental procedure

Both LNO and BTO films were fabricated on (001) Si substrates by multi-targets radio frequency (rf) co-sputtering method. Because of the insulating nature of the ferroelectric oxides, like BTO used here, the basic dc-sputtering doesn't work. Charges will build up at the surface of the insulating target and will eventually cancel out the external electric field. One solution to this problem is to apply an alternating electric field instead of a dc electric field. However, if the introduced alternating electric field is of low frequency, both electrons and ions can respond to the applied oscillating field, which will result in the damage of the film. For example, during one half of the cycle, sputtering of the cathode targets happens and during the other half cycle, sputtering of the anode substrates happens, which is known as re-sputtering and is detrimental to film growth. Radio frequency field is a good way to overcome this shortcoming, since the heavy Ar^+ ions cannot respond to a rf electric field while the electrons still can. Therefore, sputtering of the insulators is achievable without re-sputtering the deposited film [23-25]. Here, we utilize electromagnetic fields with a frequency of 13.56 MHz to generate the plasma. As shown in Fig. 1(a), the target is connected to the powered electrode as a "cathode", while the rest of the vacuum chamber, including substrates, is normally grounded as the "anode". The rf electric field generates plasma, but only the electrons are light enough to respond to the alternating filed at this frequency. The heavy Ar^+ ions "see" only the average electric field. The smaller area of the

Epitaxial Integration of Ferroelectric BaTiO$_3$ with Semiconductor Si:
From a Structure-Property Correlation Point of View
365

"cathode" results in a higher electron concentration during each half cycle compared to the electron concentration at the "anode", which will result in a net negative dc bias between the target and the substrate in a few cycles. It is this self-generated negative dc bias at the target that will drive and accelerate the Ar$^+$ ions towers the target, causing the sputtering of the target surface atoms.
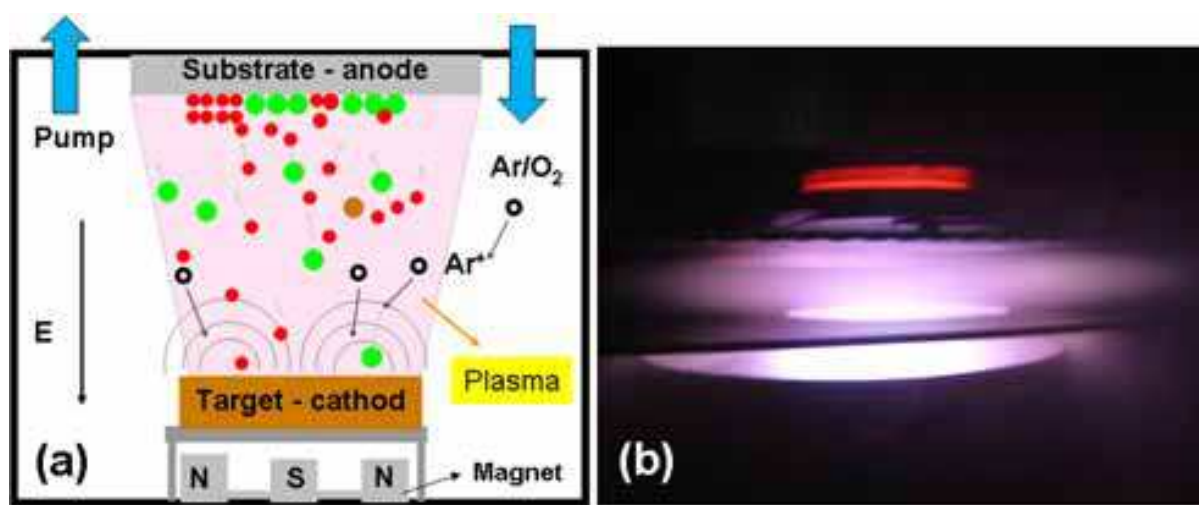

Fig. 1. (a) Schematic diagram of rf sputtering process. (b) The actual arcing and deposition process of our rf sputtering system

Si (100) wafers were first cleaned ultrasonically in acetone and methanol for 10 min each. During the whole deposition process base vacuum was below 3×10^{-4} Pa and substrate temperature was maintained at 600 °C. The deposition was generally performed either in vacuum or in a mixed atmosphere of oxygen (1.0 Pa) and argon (3.0 Pa) to prevent oxygen loss. After deposition, the as-deposited films were cooled down to room temperature (RT) in the mixed sputtering atmosphere and no additional annealing was applied. Typical puttering parameters are summarized in the following Table 1.

	LNO film	BTO film
Sputtering gas	Ar+O$_2$	Ar+O$_2$
Gas pressure	Ar:O$_2$ = 3:1	Ar:O$_2$ = 3:1
Input power (W)	71	67
Substract T (°C)	600	600
Target diameter (mm)	60	60
Deposition rate (Å/s)	1.0	0.8

Table 1. Typical sputtering conditions for LNO and BTO films

Specifically, LNO target was made by precursors of lanthanum nitrate hexahydrate and nickel acetate in the following method. First, lanthanum nitrate and nickel acetate powders were washed in distilled water, respectively. After drying, both of them with the precise stoichiometric ratio 1:1 were dissolved by acetic acid in a magnetic beater at a constant

temperature of 70 °C to give a homogeneous solution until it became steadily clear and transparent. Then, the homogeneous solution formed was dried at 200 °C with 4 h for the elimination of water and acetate, 600 °C with 4 h for the elimination of nitrate. The sintering process was carried out at 800 °C in an open atmosphere for 10 h. This process was repeated twice with intermittent grinding in an agate mortar. Finally the mixture was pelletized to the target shape, added with ethylene glycol (3% v/v) (in order to increase the viscosity of the powder), and sintered at 800 °C for 24 h.

Microstructure and crystallographic orientation of the films were characterized by θ-2θ scans of a 30 kV X-ray diffractometer (XRD, D/max2200PC, Rigaku) with Cu K_{α} radiation and a Ni filter. Grain size and surface morphology of the films were studied by atomic force microscope (AFM, SPI 3800N, SEIKO), performed at the tapping mode with sharp tips (BS-ElectricMulti75, resonance frequency of 75 Hz). Grain size distribution, interfaces and ferroelectric domains for the BTO/PLNO were observed by a 200 kV field emission high-resolution transmission electron microscope (HRTEM, 2100F, JEOL). Plan-view and cross sectional TEM samples were prepared through a standard procedure of cutting, gluing, slicing, grinding, dimpling, and finally ion milling, see Fig. 2(a) ~ (c). Electrical transport properties of the LNO films were evaluated by a domestic made four-probe testing system. Temperature dependent dielectric permittivity
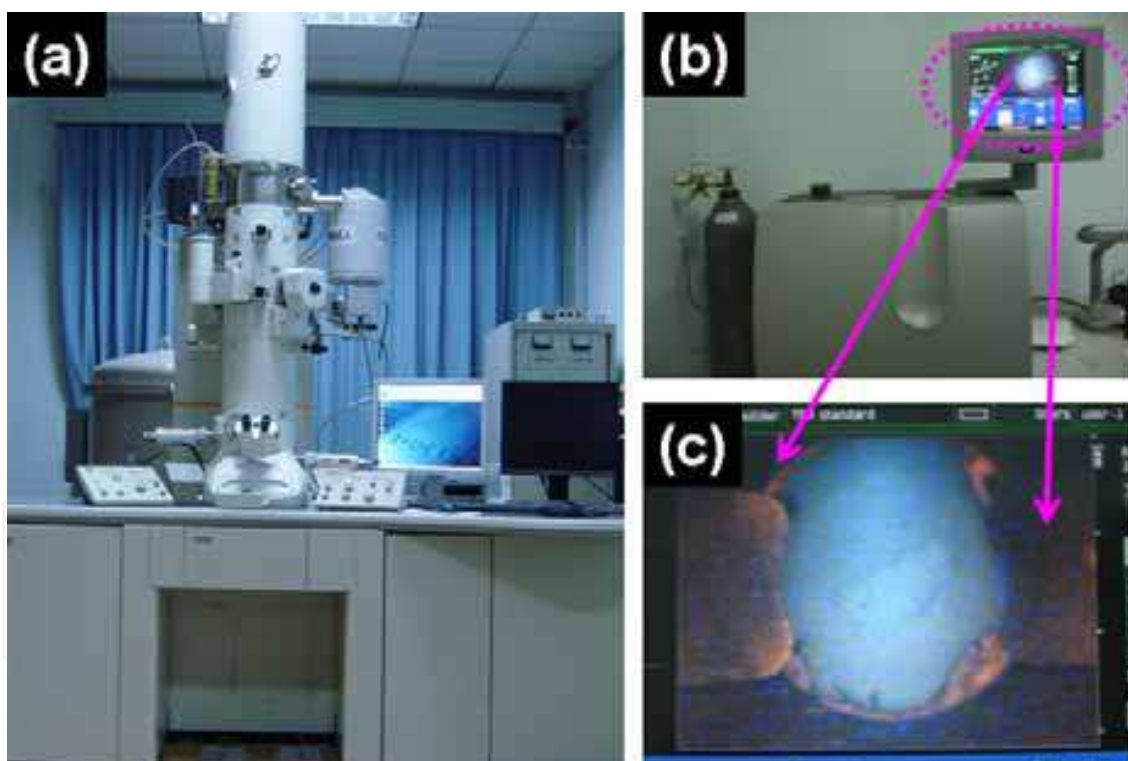

Fig. 2. (a) JOEL-2100F TEM system, (b) RS101 multi-functional ion milling system, and (c) the TEM sample was in-situ milling by the sputtering gun.

and dielectric loss for various BTO films were measured using an impedance analyzer (HP4194A, Hewlett-Packard Ltd.), at a bias voltage of 0.1 V, in the frequency range of 100 Hz–120MHz. Hysteresis loop was measured under an alternative electric field using a ferroelectric test system (TF 2000 analyzer, axiACCT, Germany). The electric properties were measured in a typical plate-capacitor setup. The top electrode layer was LNO, which was

fabricated with the same deposition parameters as the bottom LNO and then patterned with a stainless iron mask of 200 mm in thickness and 1mm in diameter.

3. Growth mechanism and crystal structure

Fig. 3(a) shows typical XRD pattern for LNO films deposited on Si (100) substrate. As can beseen LNO film possesses a pseudocubic crystal structure with a (100) preferred orientation. In fact, the lattice parameters for cubic silicon are $a = b = c = 5.43$ Å. But for pseudocubic LNO, they are $a = b = c = 3.84$ Å. Although there is no direct lattice match between (100) silicon and (100) LNO, the diagonal length for the pseudocubic LNO equals to $\sqrt{2} a = 5.43$ Å, indicating that the atomic arrangement along the (110) direction for LNO matches well with that along the (100) direction for silicon. As a result, it can be inferred that the LNO films have grown epitaxially, when deposited on (100) Si wafers, via a 45° of azimuth angle rotation in a-b plane of LNO, leading to the formation of the highly (100)-oriented LNO films on the (100) Si substrate. Fig. 3(b) shows the schematic map of orientation and interatomic spacing relationship between Si (100) and LNO (100) lattices, it can be obtained that the epitaxial relationship is (001) LNO || (001) Si and [110] LNO || [100] Si. From AFM observation, it can be seen that the LNO films exhibit a uniform and dense microstructure with grain size about 30 nm, as shown in the insert of Fig. 3(a). The root-mean-square (rms) roughness measured from the figure is 8.75 nm over the area of 1μm×1μm, indicating that the films has a very smooth surface.
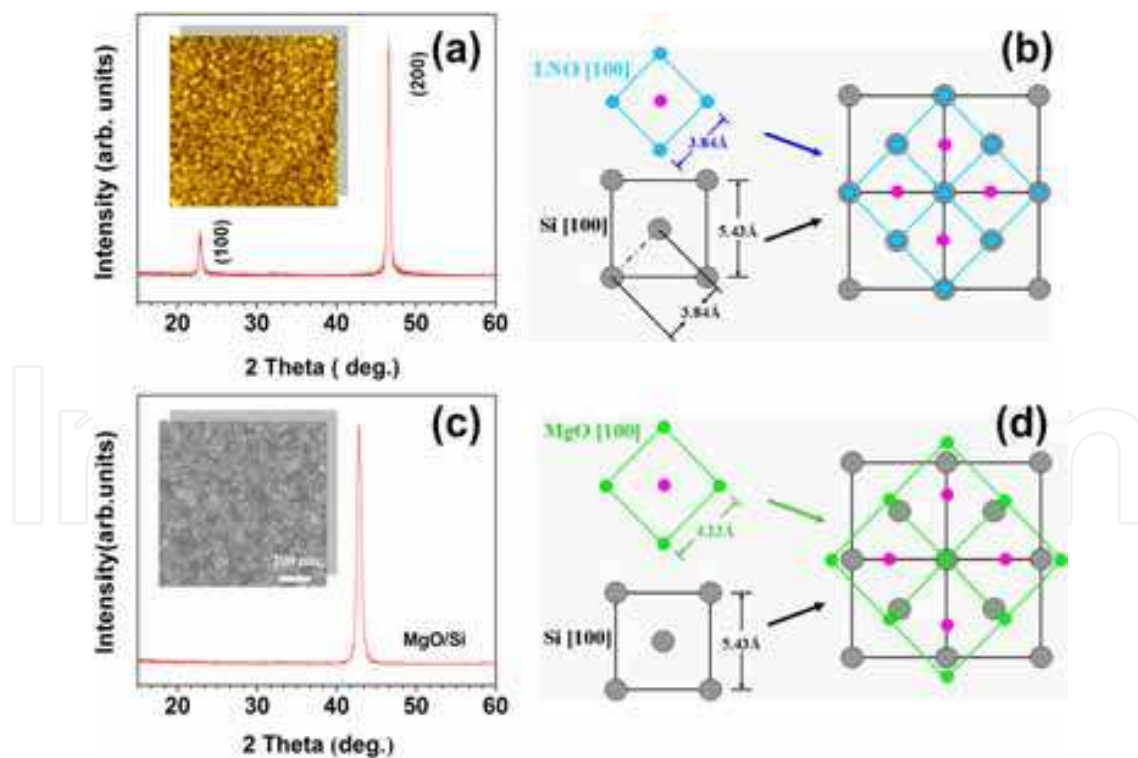

Fig. 3. XRD patterns of LNO (a) and MgO (c) films deposited on Si(001) substrate. (c) and (d) are schematic maps of orientation and interatomic-spacing relationship of LNO/Si (100) and MgO/Si (100), respectively. Insets in (a) and (c) are AFM and SEM images for LNO and MgO films, respectively.

Since magnesium oxide (MgO) is also a common buffer layer for the growth of thin film ferroelectric oxide materials and it exhibits superior stable chemical property, we also grow MgO films on Si substrate. Fig. 3(c) presents the XRD pattern of MgO(400nm)/Si. Obviously, MgO also exhibit seemingly high (100)-orientation and a good crystallinity (see inserted SEM image in Fig.3(c)). This can also be understood in term of the lattice matching between MgO and Si. Cubic MgO has a lattice constant of 4.23 Å, the lattice mismatch between MgO and Si in [100] direction is thus ~ 22.1%. This value is still too large to maintain a film with good crystallographic quality. On the other hand, as illustrated in Fig. 3(d), the lattice mismatch between the two materials in [110] direction is decreased to 10.2%, which is an acceptable value for the growth of highly oriented MgO film. However, it should be noted the lattice mismatch of MgO/Si is still significantly larger than that of LNO/Si, which will affect the structural quality of the upper ferroelectric BTO films.

Fig. 4(a) show XRD patterns of BTO films grown on bare Si(001) and MgO/Si(001) substrates, respectively. As can be seen, the BTO film grown directly on Si shows a typical random perovskite phase with no (100) orientation due to the large lattice mismatch between BTO (3.99 Å) and Si (5.43 Å). Insertion of a MgO intermediate layer between BTO and Si improves the (100) texture orientation of BTO film hugely and the BTO film also exhibit a good crystalline structure (Fig. 4(b)). However, a tiny BTO (110) peak still presents in the XRD pattern, indicating that MgO is not an ideal buffer layer material for highly (100) orientation growth of BTO because of its large lattice mismatch with Si substrate, as mentioned above. In contrast, BTO film grown on LNO/Si exhibits a
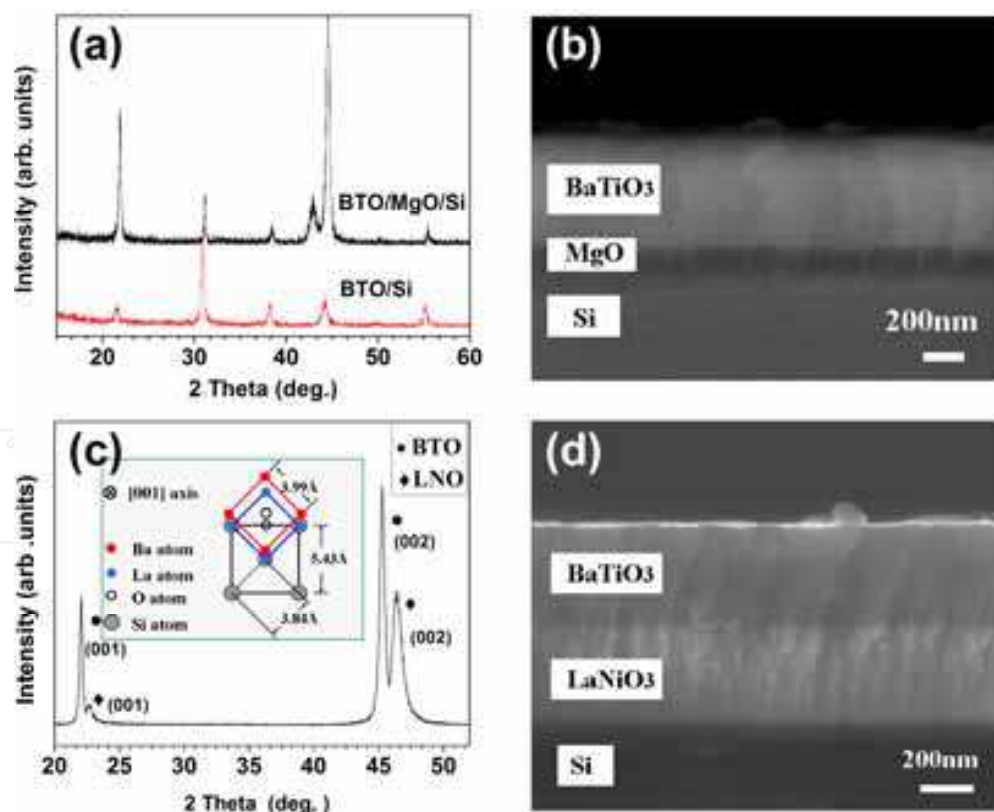

Fig. 4. (a) XRD patterns of BTO films grown on bare Si(001) and MgO/Si(001) substrates. (b) Cross-sectional SEM image for BTO/MgO/Si. (c) XRD pattern of BTO/LNO/Si(001). (D) (b) Cross-sectional SEM image for BTO/LNO/Si.

Epitaxial Integration of Ferroelectric BaTiO₃ with Semiconductor Si:
From a Structure-Property Correlation Point of View
369

pure (001)-orientation structure, as indicated in Fig. 4(c). Since lattice mismatch between BTO and LNO is only ~ 3.76%, the pre-deposited LNO film will act as a seed layer for the (001) orientation growth of the BTO layer. An atomic arrangement relationship among the three kinds of lattices (Si substrate, conductive LNO and ferroelectric BTO) is also described in Fig. 4(c). In the film growth process, this little lattice mismatch is very important as it can induce a proper internal stress energy, which will not only maintain the (100) orientation growth but also induce an additional tetragonal distortion and change the ratio of c/a for the ferroelectric film. Fig. 4(d) shows the typical cross-section image of BTO/LNO/Si structure, in which both the BTO and LNO layers display dense microstructure and columnar grains extending over the entire film. The interface between LNO layer and BTO layer is distinct, smooth and of good quality.

The structural quality of BTO films on LNO/Si substrates is further demonstrated by in-plane XRD measurement and HRTEM cross-sectional interface observation. Fig. 5(a) is a typical in-plane {110} φ scan of the BTO film on LNO/Si. The presence of four accurately uniformly spaced (110) peaks reveals the fourfold symmetry of the film, confirming the good in-plane alignment between BTO film and LNO/Si substrate. The cross-sectional HRTEM image of the interface between [001] - LNO and [001] - BTO is presented in Fig. 5(b), along with the low magnification image for the bi-layer (inset). The consecutive lattice image shown in the figure proves the epitaxial growth relation between the BTO thin film and the LNO/Si substrate within a "cube-on-cube" fashion. An epitaxial growth relationship is as follows: (001) [001] BTO || (001) [001] LNO || (001) [001] Si and [110] BTO || [110] LNO || [100] Si.
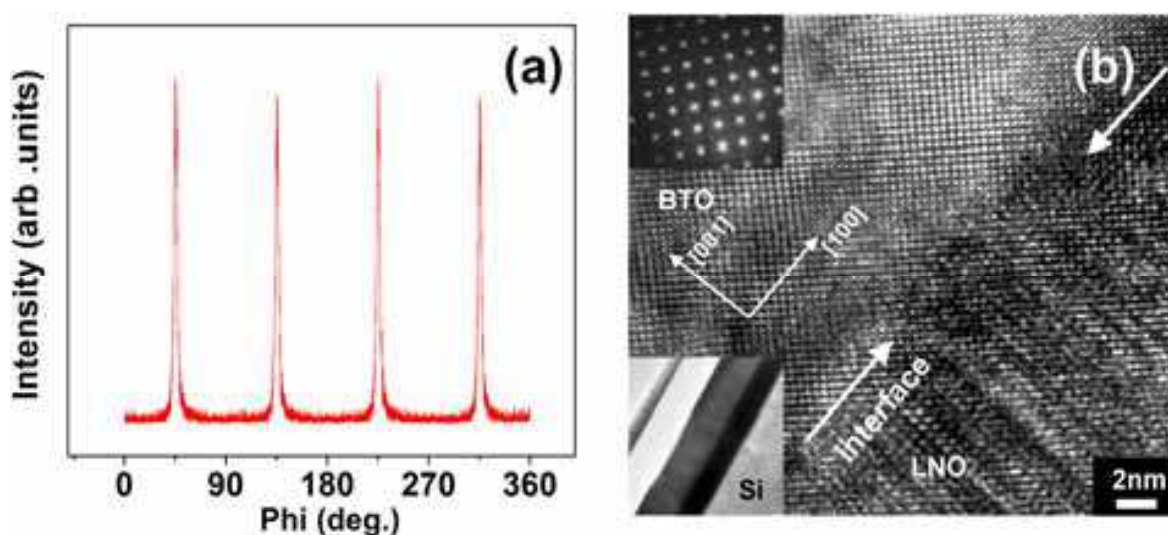

Fig. 5. (a) Typical in-plane {110} φ scan of the BTO film on LNO/Si. (b) HRTEM cross-sectional image of the BTO/LNO interface on Si.

Based on above discussions, the LNO film is a more suitable buffer layer for the growth of high quality BTO films. Since LNO films are also used as electrodes, we have investigated their electric properties. When the film thickness is 400 nm, the resistivity for the highly (100)-oriented LNO film at room temperature is 1.2×10^{-3} Ω·cm. Previous reports have shown that the resistivity for those highly (100)-oriented LNO thin films varies the range of $4.5 \times 10^{-4} \sim 1.0 \times 10^{-2}$ Ω•cm, depending on fabrication processes [26,27]. The variations in the resistivity could be attributed to composition deviation from typical ABO₃ chemical

stoichiometry especially the oxygen loss, which were influenced by the deposition method and temperature. The lower resistivity of around 1.2×10^{-3} $\Omega \cdot$cm obtained in this work indicates that the highly (100)-oriented LNO films prepared by sputtering could be used as both buffer layer and bottom electrode, which is of significance for fabricating highly-oriented ferroelectric thin films.

4. Grain size effect

It is known that both microstructure and properties of ferroelectric films are dependent greatly on fabrication processes [28-31]. The extrinsic parameters are also assumed to be responsible for variations in microstructure dependence of ferroelectricty, and might be the reason for a broad dispersion in some data such as critical size below which ferroelectricity is eradicated. For example, in the last two decades, there had been a variety of different experimental critical thickness for epitaxial ferroelectric thin films [32-37]. However, recent theoretical and experimental studies have implied that there is no intrinsic thickness limit for ferroelectricity in thin films with thickness down to even several unit cells [38,39]. While for ferroelectric polycrystalline films, nano-particles, or nano-ceramics, there is still no unambiguous conclusion that if there exists a critical grain size responsible for the disappearance of the macroscopic ferroelectricity. To investigate the effect of grain size on the ferroelectric properties of BTO films, it is important to control the experiment so that the only different parameter for different BTO films is variable size of grains. The ferroelectric BTO thin films of 200 nm were first deposited onto the LNO buffer layers at room temperature. The as-deposited films were then annealed in an open-air atmosphere with different temperatures ranging from 400 ~ 800 °C for 2 hours in order to obtain different grain size.
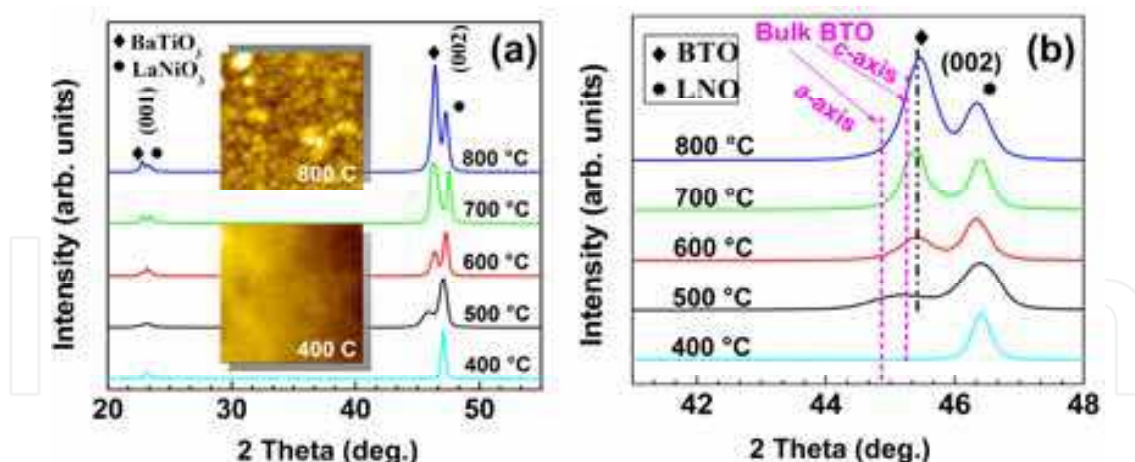

Fig. 6. (a) XRD patterns of the BTO films annealed at different temperatures ranging from 400°C to 800°C, (b) magnified view of XRD patterns in Fig. 6(a)

Fig. 6 (a) shows the XRD patterns of the BTO films annealed at several different temperatures. When the annealing temperature is 400 °C, only (100) and (200) peaks for LNO can be observed and no any other peaks related with BTO can be identified, indicating that the BTO film remain an amorphous structure at the temperature. When the annealing temperature is increased to 500 °C, a broadened (200) peak ascribed to the BTO start to appear. With further increasing the annealing temperature, the peaks become much sharper and are gradually

Epitaxial Integration of Ferroelectric BaTiO₃ with Semiconductor Si:
From a Structure-Property Correlation Point of View

371

intensified. From the results, it can be obtained that the BTO films start to crystallize at 500 °C from the amorphous phase and grow into a (100) preferred orientation on the LNO (100) buffered Si substrates as the annealing temperatures increase. The surface morphologies of BTO films annealed at different temperatures had also been analyzed by AFM observations, as shown in inset of Fig. 6(a). The 400 °C -annealed BTO film exhibits an amorphous structure without the formation of any distinct grains on the surface and increasing annealing temperature will increase the BTO grain size, which agrees well with the XRD results.

From the magnified view of XRD patterns in Fig. 6(b), the lattice constants as well as strain states for both BTO and LNO layers can also be extracted. The (002) peaks for all the LNO layers are positioned at the same diffraction angel, indicating the LNO films possess same lattice constant, which is calculated to be 3.91 Å. Compared with that of bulk LNO (3.84 Å), the larger value reveals that LNO films are under tensile strain. On the other hand, compared with the 2θ peak position of bulk BTO (purple dashed lines), these BTO (002) 2θ diffraction peaks are shifted to higher angles, indicating a decease in the out-of-plane lattice constants and an increase in the in-plane lattice constants in the BTO films. Since the LNO layer is very thin compared with Si, so the shift is suggested to be the result of the thermal strain induced during the cooling process caused by the difference of thermal expansion coefficients between BTO layer and Si substrate. This corresponds well with the experimental strain states for BTO when incorporated with Si substrate [40,41]. The strain state and its effect on the structure and properties of ferroelectric BTO films will be further discussed in the part 5. Nevertheless, as the (002) peaks for all the BTO layers are almost at the same position (black dashed line), so the BTO layers are under same strain state in spite of different annealing temperature.
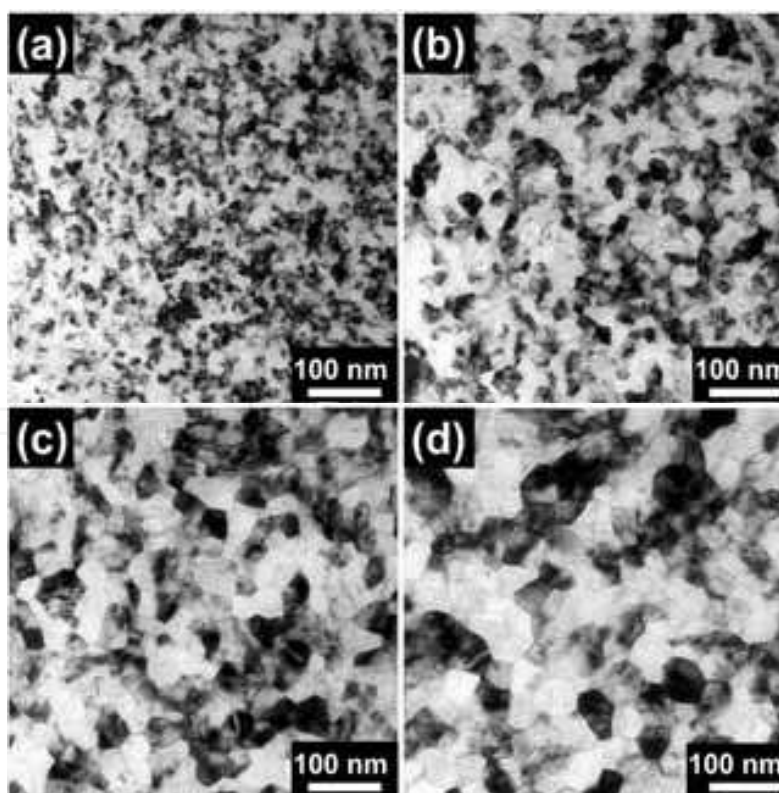

Fig. 7. Plan-View TEM images of the BTO film annealed at different temperatures: (a) 500°C, (b) 600°C, (c) 700°C and (d) 800°C. The inset is the electron diffraction arc for the 800°C -annealed film.

Microstructures for the annealed films were characterized by plan-view TEM observations, as shown in Fig. 7(a) ~ (d). It is clearly seen that the films annealed at temperatures ≥500 °C are crystallized and featured as uniform and cracks-free. The grain size is increased with increasing the annealing temperatures, changing from 14 to 55 nm in diameter. It is noted that the BTO films in this work exhibit much smaller grain sizes as compared to other reported BTO films [42,43]. The difference is considered to be the result of the influence of microstructure of the LNO buffer layer. It is known that grain size for a newly formed crystal is dependent on the nucleation rate and the growth rate, respectively. In this work, the LNO buffer layer with very fine grain size of 20 ~ 30 nm was used as seed layers for the ferroelectric BTO films. The grain boundaries in the LNO buffer layers will act as nucleation sites for the crystallization of the BTO films during the annealing processes. The smaller grain size of the LNO film leads to more nucleation sites for the crystallization of BTO films and, as a result, the BTO films grow into a microstructure characterized by fine and uniform grains.

Room temperature ferroelectric hysteresis loops of the BTO films annealed at different temperatures are displayed in Fig. 8(a). For BTO films annealed at 600 °C and above, obvious hysteretic shape of polarization vs electric field (P-E) curves are obtained. With increasing the annealing temperature, the P-E hysteresis loop starts to become much more erect and saturated, showing a typical ferroelectric characterization. The obtained remnant polarization (P_r) for 800 °C -annealed BTO is 2.0 μC/cm², similar to the values of other polycrystalline BTO films, e.g. 2.0 μC/cm² on Pt/Ti/TiO$_x$/Si by Thomas *et al.* [44] and 1.0 μC/cm² on Pt/SiO$_2$/Si by Huang *et al.* [45]. However, compared with the value for BTO single crystal (24 μC/cm²) or other epitaxial BTO films [46,47], the P_r is still much lower, probably due to fine grain size and the formation of in-plane tensile
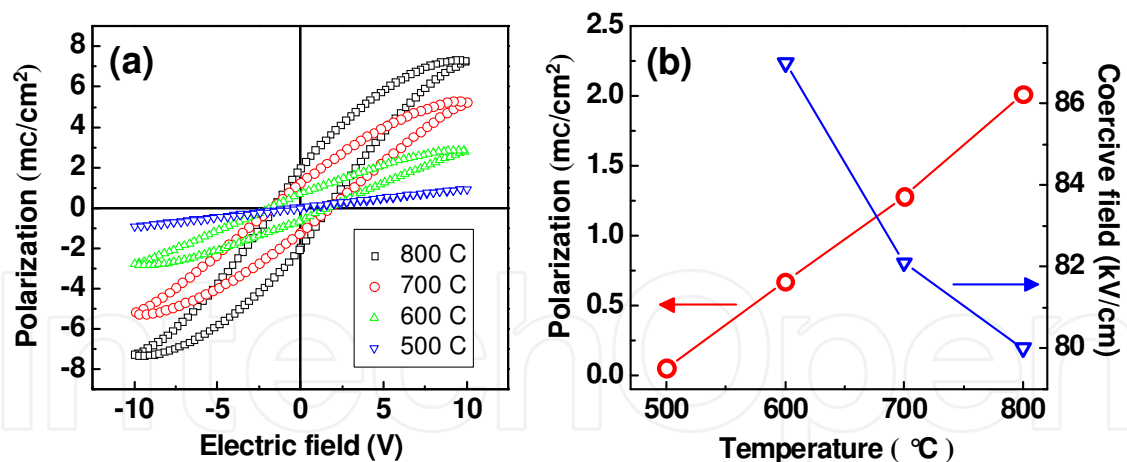

Fig. 8. (a) Hysteresis loops of the BTO films after annealing at different temperatures. (b) Annealing temperature dependence of the remnant polarization and coercive field for the BTO films.

strain state on the Si substrate, as had been obtained by the XRD analysis. On the other hand, for BTO film with the finest grain size of 14 nm (annealed at 500°C), it still exhibits some hysteresis characteristics with P_r ~ 0.08 μC/cm², although it is not obvious and shows almost linear dependence of P(E). This corresponds well with the recently reported experimental results that the ferroelectricity does exist in nanocrystalline BTO ceramics with ultra fine grain size of 30 nm [48], 22 nm [49], and even 8 nm [50]. However, the significantly

Epitaxial Integration of Ferroelectric BaTiO$_3$ with Semiconductor Si:
From a Structure-Property Correlation Point of View

373

reduced P_r is indicative of a strong suppression of macroscopic ferroelectric character in the 14 nm BTO film, which may arises from either the frozen domain structure under an external field by grain boundary effects, such as the clamping of the domain walls and the hindrance of polarization switching, or the depolarization field originated by the low permittivity nonferroelectric grain boundaries [49]. Besides, the low crystallinity of 500 °C - annealed BTO is also a possible reason for the obtained low P_r. On the other hand, it should be noted that from XRD patterns for the BTO films, the separation of diffraction peaks (200) and (002) was not observed for all the annealed films. Meanwhile, the ferroelectricity is known to be attributed to the formation of tetragonal structure in materials. Thus, the different properties for the BTO thin films annealed at different temperatures suggest that a pseudocubic structure be formed in the BTO films having a larger grain size. The idea of the pseudocubic phase is based on a core-shell grain model in which individual grains consist of a cubic shell and a tetragonal grain interior [51]. Internal strains in tetragonal structure caused by the formation of nano-scale grains are believed to be responsible for its change to the so-called pseudocubic phase [52,53]. It can be considered that the obvious ferroelectricity observed in this work for the films after annealing at or above 600 °C is attributed to the formation of the pseudocubic phase, while the strong restrained ferroelectricity for the film annealed at 500 °C is due to the suppression of the tetragonal core caused by the smaller grain size.

To further study the change of the ferroelectricity with different grain size, Fig. 8(b) plots the P_r and coercive field (E_c) of the BTO films as a function of annealing temperatures. As the annealing temperature increases, the remnant polarization increases while the coercive field decreases. Since all the films have the same thickness and the same in-plane tensile strain state, their grain size is then responsible solely for their different ferroelectric behaviors. Theoretical calculations have demonstrated that the density of 90° domain walls is inversely proportional to the square root of the grain size [54]. It means that the density of domain walls is increased with the decrease of annealing temperature, and consequently a distance dependent repulsive force between neighboring domain walls is enhanced. This leads to a reduction of the mobility for domain walls and more difficulty in domain orientation, resulting in the reduction of P_r and the increases of E_c.

5. Strain engineering and phase transition

The microstructure of the film has a great influence on the corresponding physical properties. Recently, the investigation of strain effect has become increasingly important due to its great influence on the ferroelectric phase transition, domain formation, and polarization magnitude for ferroelectric thin films. Haeni *et al*. [55] have demonstrated that a proper epitaxial strain from a DyScO$_3$ substrate can increase ferroelectric Curie temperature by hundreds of degrees and produce room temperature ferroelectricity in SrTiO$_3$ which does not originally exhibit ferroelectric property at any temperature. Enormously high remnant polarization (P_r) was also reported by Choi *et al*. [47] in relatively thick epitaxial BTO films grown on a newly developed DyScO$_3$ substrate. The P_r observed is about 70 µC/cm^2, which is almost 2.7 times higher than the spontaneous polarization of bulk BTO (P_s = 26 µC/cm^2). In this section, we show that, the strain state and the dielectric, ferroelectric as well as domain configurations of ferroelectric BTO layer on LNO/Si is critically dependent their respective film thickness, and this can actually be utilized to engineer the strain and the physical properties of BTO.

5.1 Strain modeling

For ferroelectric thin films, internal strains are mainly induced by lattice distortion due to the different lattice parameters [56] and the incompatible thermal expansion coefficients (TECs) between the film and substrate (or buffer layers) [57], to the self-induced strain of phase transition during the cooling process [58], and to the inhomogeneous defect-related strains such as impurities or dislocations [41]. However, the contribution from the later two factors can be avoided by selecting suitable materials and exploring advanced film growth techniques.

Schematic Fig. 9 illustrates the formation and evolution of the strain in a typical epitaxy film growth process. At the film growth temperature, when atoms arrive at the surface of the substrate, they will initially adopt the substrate's in-plane lattice constant to form an epitaxial film [Fig. 9(a)]. As long as the film thickness (t) is smaller than the critical thickness (h_c) of the film/substrate system, the film will keep its coherence with substrate and maintain a fully strained layer [Fig. 9(b)]. When $t > h_c$, dislocations will appear at the interface or near interface region and the whole film relaxes. However, the relaxation is a dynamic controlled process, if the film thickness is not large enough than h_c, the relaxation may only occur partially [Fig. 9(c)]. Finally, during the cooling process,
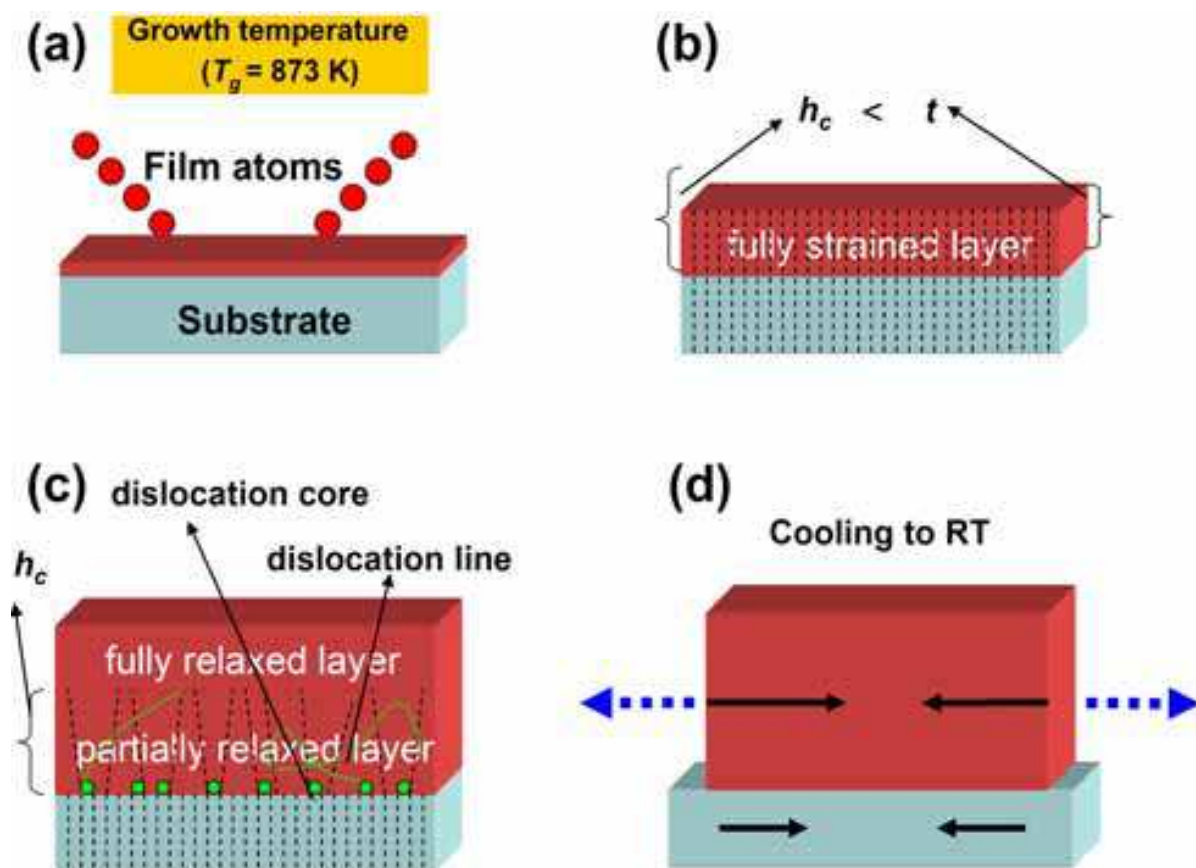

Fig. 9. An illustration of the strain formation and evolution in a typical epitaxy film growth process.

additional thermal strain may also be exerted on film due to the difference of the TECs between the film and substrate [Fig. 9(d)]. Therefore, the temperature dependent misfit strain in a thin film can be modeled simply by taking into account the combined

Epitaxial Integration of Ferroelectric BaTiO$_3$ with Semiconductor Si:
From a Structure-Property Correlation Point of View

375

contribution of the temperature dependent lattice strain [$S_m(T_g)$] and the thermal strain [$S_{therm}(T)$] [59], which can be approximated by the linear relation,

$$S_m(T) = S_m(T_g) + S_{therm}(T) \tag{1}$$

$$S_{therm}(T) = (\alpha_s - \alpha_f)(T - T_g) \tag{2}$$

where, T_g = 873 K, is the growth temperature, $S_{therm}(T)$ is the thermal strain, α_s and α_f are linear thermal expansion coefficients (TECs) of the substrate and prototypic cubic phase of the film. $S_m(T_g) = [a_s^*(T_g) - a_f(T_g)] / a_s^*(T_g)$ is the effective misfit strain of the film and substrate at T_g, $a_s^* = a_s(1 - \rho)$ is the effective lattice parameter of the substrate [60] and ρ is the dislocation density [61], which reflects the effect of strain relaxation induced by the appearance of misfit dislocations at the film/substrate interface at T_g.

For the convenience of understanding, we define an original misfit lattice strain $S_m^0(T_g)$, which means the actual original misfit strain between the as-grown film and the supporting substrate if the film does not relax at all at the growth conditions, as follows,

$$S_m^0(T_g) = [a_s(T_g) - a_f(T_g)] / a_s(T_g) \tag{3}$$

Taking into account the thermal expansion, the lattice constant of the film and substrate at T_g can be approximated by $a_f(T_g) = a_f(RT)[1 + \alpha_f(T_g - RT)]$ and $a_s(T_g) = a_s(RT)[1 + \alpha_s(T_g - RT)]$, respectively. As a matter of fact, the $S_m^0(T_g)$ does not really exist, because the film growth and relaxation occur simultaneously. However, we assume the film growth process and the strain relaxation process can occur in the following two successive steps. First, the film doesn't relax during the whole growth procedure (holding a $S_m^0(T_g)$) and then, when growth is done the relaxation process dominates and the as-grown film begins to relax only when the accumulated $S_m^0(T_g)$ exceeds the critical relaxation requirements. In this picture, the $S_m(T_g)$ in equation (1) can be thus equivalently and much more schematically divided into the combination of an original lattice strain $S_m^0(T_g)$ at T_g and a strain variation due to the formation of misfit dislocations [$S_{dis}(\rho, T_g)$] during relaxation,

$$S_m(T_g) = S_m^0(T_g) + S_{dis}(\rho, T_g) \tag{4}$$

In addition, structural factors such as growth defects, crystallinity, and oxygen vacancies may also contribute to the $S_m(T)$ [41], which is denoted by S_{other} in the following expression.

$$S_m(T) = S_m^0(T_g) + S_{dis}(\rho, T_g) + S_{therm}(T) + S_{other} \tag{5}$$

By analyzing the first three terms on the right side of equation (5), we can roughly estimate the final strain in the obtained film.

We start from the LNO buffer layer. Fig. 10 (a) shows the XRD patterns for various LNO films with different thickness. It is obvious the LNO (200) peak shifts toward high angles with increasing the film thicknesses, indicating a decrease in the lattice constant. Fig. 10 (b) shows the LNO thickness dependent lattice constant ($a = 2d_{002}$) and misfit strain ($S_m = (a - a_0)/a_0$, where a_0 is the lattice constant for freestanding bulk LNO) obtained from the XRD result at RT. As can be seen, the lattice parameters decrease with increasing the LNO thickness and become close to the bulk value (3.84 Å) for 600 nm LNO film.
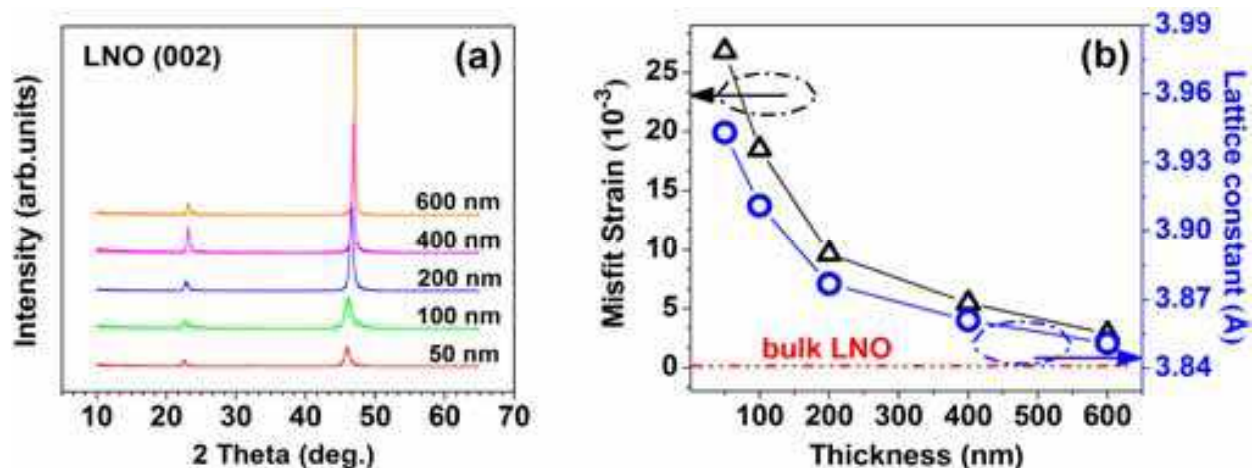
Fig. 10. (a) XRD patterns for LNO films with different thicknesses. (b) Calculated LNO thickness dependence of misfit strain and lattice constant, along with the lattice constant for bulk LNO.

For the LNO film directly grown on a Si substrate, using equations (3), we can calculate the origin misfit lattice strain and $S_m^0(T_g) \sim -3.68 \times 10^{-3}$. Based on elastic theory, the $S_m^0(T_g)$ will be fully relaxed by the formation of misfit dislocations at the film/substrate interface when the thickness of the film (h) is larger enough than the critical thickness (h_c) [62],

$$h_c = \left(\frac{b}{f}\right)\left[\frac{1}{4\pi(1+\upsilon)}\right]\left[\ln\left(\frac{h_c}{b}\right)+1\right] \qquad (6)$$

where υ is the Poisson's ratio, f the relative misfit, and b the Burger's vector of misfit dislocations. Due to lack of υ value for LNO, here we simply assume $\upsilon = 0.3$, a typical value for perovskite oxides [63], and h_c is estimated to be on the order of 23 nm for a 0.5%-misfit film. Considering that the film thickness $t >> h_c$, so the $S_m^0(T_g)$ will be fully relaxed by $S_{dis}(\rho, T_g)$, making $S_m^0(T_g)$ and $S_{dis}(\rho, T_g)$ negligible. The $S_m(T)$ in equation (5) is therefore attributed mainly to the thermal strain $S_{therm}(T)$ and S_{other}. Generally, due to large difference in TECs between LNO and Si, the induced thermal strain will make the LNO film under a tensile strain state with an enlarged lattice constant at room temperature, which is consistent with the former XRD results. Using equation (2) the thermal strain $S_{therm}(T)$ at RT for the LNO is estimated to be $\sim 3.91 \times 10^{-3}$, while the XRD analysis shows that $S_m(RT)$ for the LNO films is decreased from 26.82×10^{-3} to 2.865×10^{-3}, as shown in the inset, when the thickness varies from 50 nm to 600 nm. The result also indicates that a strain in the LNO films induced by the Si substrate can be fully relaxed by increasing their thicknesses to a certain extent. Note that the difference between $S_m(RT)$ values and the thermal strain also confirms the contribution of structural parameters (S_{other}), as represented in equation (5).

5.2 Tensile strained BTO

Fig. 11(a) shows the XRD patterns for 200 nm BTO films grown on the 100 nm LNO buffered Si. In order to determine the in-plane lattice alignment and in-plane constant of BTO, samples were placed on a tilted holder with a set azimuth angle of $\psi = 45°$, so that the (101) and (202) crystal planes are parallel to the detected surface of the films. As a result, the reflections for (101) and (202) planes in the film will become much easier to satisfy the

Epitaxial Integration of Ferroelectric BaTiO$_3$ with Semiconductor Si:
From a Structure-Property Correlation Point of View

377

Prague's Law, $2d\sin\theta = \lambda$ (d is the lattice spacing, θ the diffraction angle and λ the x-ray wave length) [64], in the x-ray detecting process and obvious diffraction of (101) and (202) planes will occur at their own characteristic diffraction angle. The 45 $^\circ$ tilted XRD θ - 2θ scans for BTO/LNO bi-layers are shown in Fig. 11(b). It is seen that only (101) and (202) reflections for LNO and BTO films are detected, implying the in-plane lattice alignment between [110] LNO and [110] BTO. Using lattice spacing d_{002} and d_{202} obtained from the Prague's Law ($d = \lambda/2\sin\theta$), the out-of-plane lattice constants ($a_\perp$) and in-plane lattice constants ($a_{||}$) for BTO can be calculated by the following equations [65],
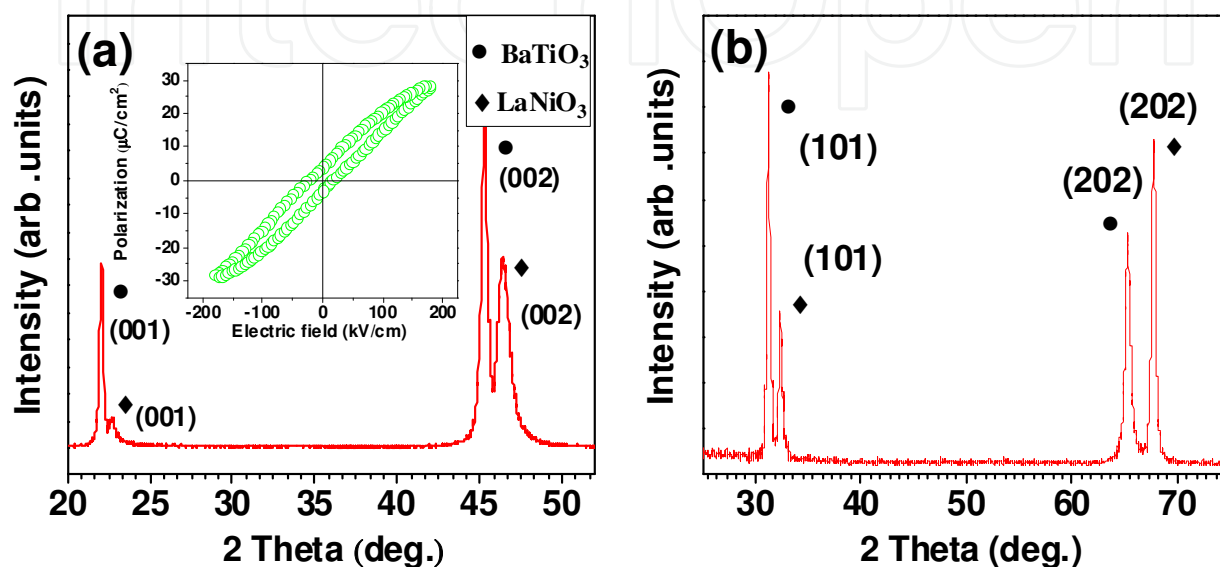
Fig. 11. (a) XRD patterns for 200 nm BTO thin film deposited on 100 nm LNO-buffered Si substrate. Inset shows the room temperature ferroelectric hysteresis loop for this BTO film. (b) 45° tilted in-plane scan for the BTO/LNO bilayer films.

$$a_\perp = 2d_{002} \tag{7}$$

$$a_{||} = \frac{2}{\sqrt{\dfrac{1}{d_{202}^2} - \dfrac{1}{d_{002}^2}}} \tag{8}$$

The obtained $a_\perp$ and $a_{||}$ for 200 nm BTO are 4.001 and 4.077 Å, respectively. Compared with bulk BTO (a = 3.992 Å and c = 4.036 Å), the BTO films are elongated along a-axis and compressed along c-axis. Besides, as out-of-plane lattice constants are always smaller than the in-plane lattice constants for both BTO films, thus it can be inferred that the BTO films are under an in-plane tensile strain state. Inset of Fig. 11(a) shows room temperature polarization and capacitance with electric field at 1 kHz. The small remnant P_r indicates that the film is nearly in an in-plane polarization state, that is, the polarization vectors mainly parallel to the film surface.

The temperature dependent dielectric permittivity and dielectric loss for the bilayer films were shown in Fig. 12(a). Over the temperature region, two broad but obvious peaks for the dielectric permittivity and dielectric loss are detected at 30 °C and 170 °C, respectively. This indicates that two phase transitions have occurred. The dielectric response can be explained

by the misfit strain-temperature phase diagrams theory [66-71] for an epitaxial polydomain ferroelectric film grown on a "tensile" substrate. As shown in Fig. 12(b), the polydomain ferroelectric films have different phase states and domain configurations compared to epitaxial single-domain film or bulk materials. This results in the contribution of an extrinsic response (domain-wall movements) together with the intrinsic response (substrate induced strain) to the dielectric response in a small signal dielectric measurement in the plate-capacitor setup. The temperature dependent misfit strain can be approximated by equation (1). Since BTO film is pretty thick, the contribution of lattice strain can be neglected, and the total strain is subjected solely to the thermal strain. Thus, the misfit strain (S_m) at the ferroelectric phase transition temperature (443 K) is estimated to be $(\alpha_s-\alpha_f)(T-T_g) \sim 3.87 \times 10^{-3}$, which just lies in the predicated $a_1/a_2/a_1/a_2$ polydomain region [66]. It can be obtained that, when the film is cooled down from the deposition temperature to Curie temperature, a second order phase transition from cubic parelectric to pseudo-tetragonal $a_1/a_2/a_1/a_2$ ferroelectric phase occurs, leading to the appearance of the broad dielectric peak in the temperature-dependent dielectric curves. On the other hand, the second permittivity peak at 30 °C is suggested to be the result of the structural phase transition between the $a_1/a_2/a_1/a_2$ and $ca_1/ca_2/ca_1/ca_2$ polydomain states that is accompanied by the appearance of the out-of-plane polarization. This is also consistent with the observation of the small P_r at room temperature.
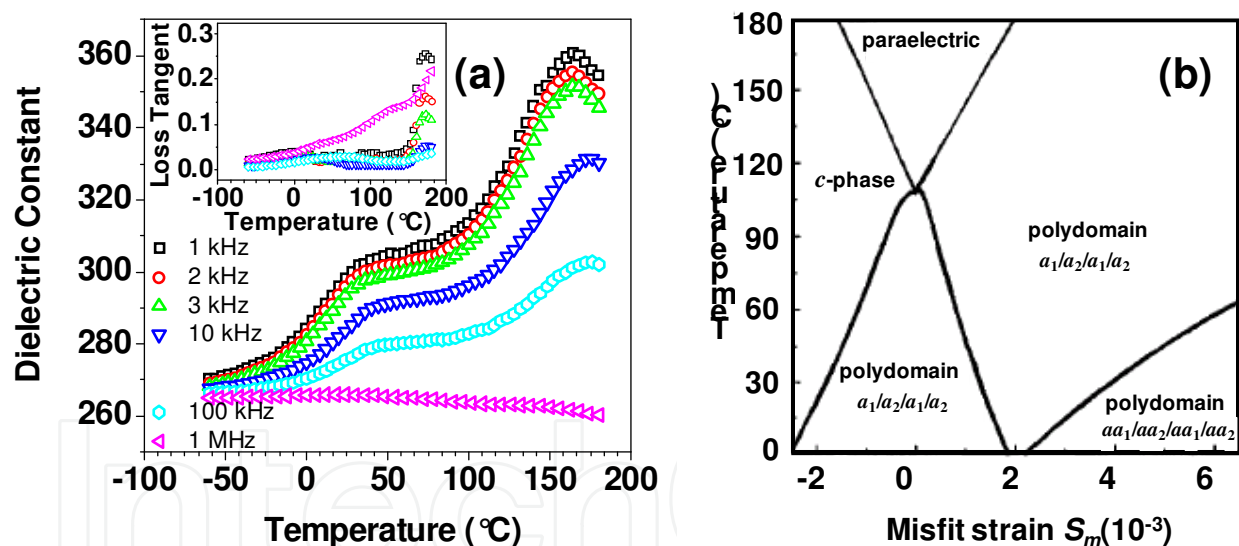

Fig. 12. (a) Temperature dependent dielectric permittivity and dielectric loss (inset) for the tensile-strained BTO film. (b) Schematic illustration of the misfit strain-temperature for BTO thin film.

Fig. 13(a) shows the plan-view HRTEM image of elastic domain pattern for the BTO film. The adjacent elastic domain walls form a coherent twin boundary lying along the surface of {110} twin planes for the minimization of in-plane elastic strain energy. Fig. 13(b) shows the cross-sectional TEM image of elastic domains. It can be clearly seen that the domain walls exhibit a blunt fringe contrast, because the polarization vectors in adjacent domains form an angle and they, as a result, are not in the same height with respect to the observation direction [72].
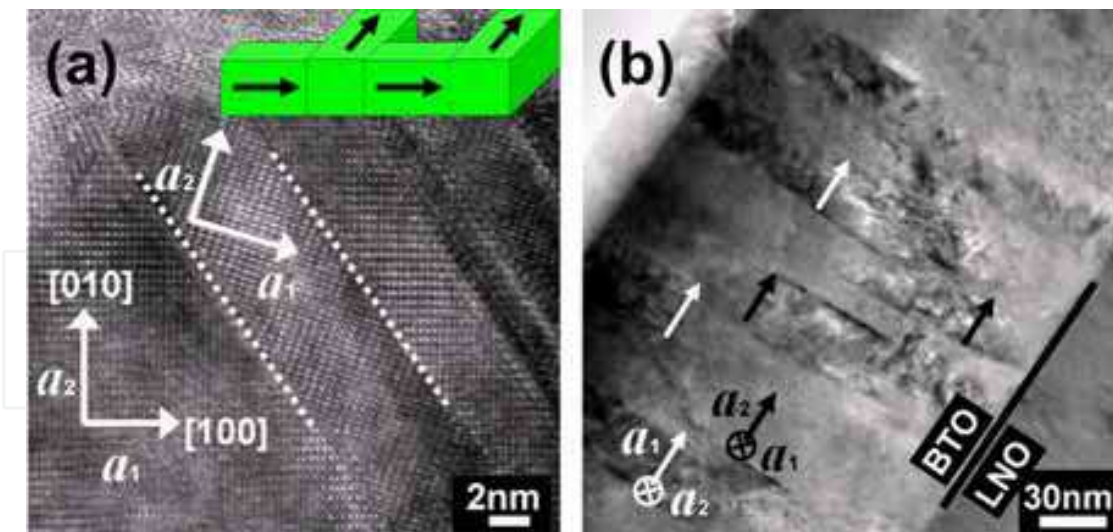
Epitaxial Integration of Ferroelectric BaTiO$_3$ with Semiconductor Si:
From a Structure-Property Correlation Point of View

379

Fig. 13. (a) HRTEM plan-view image of elastic domain configurations, (b) cross-sectional image of elastic domains.

5.3 Compressive strained BTO

Fig. 14(*a*) and 14(*b*) show the XRD patterns of normal and 45°tilted θ-2θ scans of BTO(100 nm)/LNO(600 nm)/Si. Using above mentioned method, the in-plane and out-of-plane lattice constants for the BTO film are calculated to be a = 3.955 Å and c = 4.056 Å, respectively. Then the tetragonal distortion c/a is 1.025. Compared to bulk BTO (a = 3.992 Å and c = 4.036 Å) and other tensile strained BTO films on Si substrates (e.g. c = 3.975 Å by Meier *et al*. [40]), the BTO film is elongated along *c*-axis and compressed along *a*-axis, and corresponds well with the results obtained by Petraru *et al*. in BTO (56 nm)/STO (a = 3.925 Å and c = 4.125 Å) [73]. The unit cell volume can be estimated as $V_{film} = a \times a \times c \sim 63.444$ Å^3, which is smaller than that of the bulk ($V_{teg} \sim 64.318$ Å^3 and $V_{cubic} \sim 64.722$ Å^3) [74]. Therefore, the BTO film is under a compressive strain state.
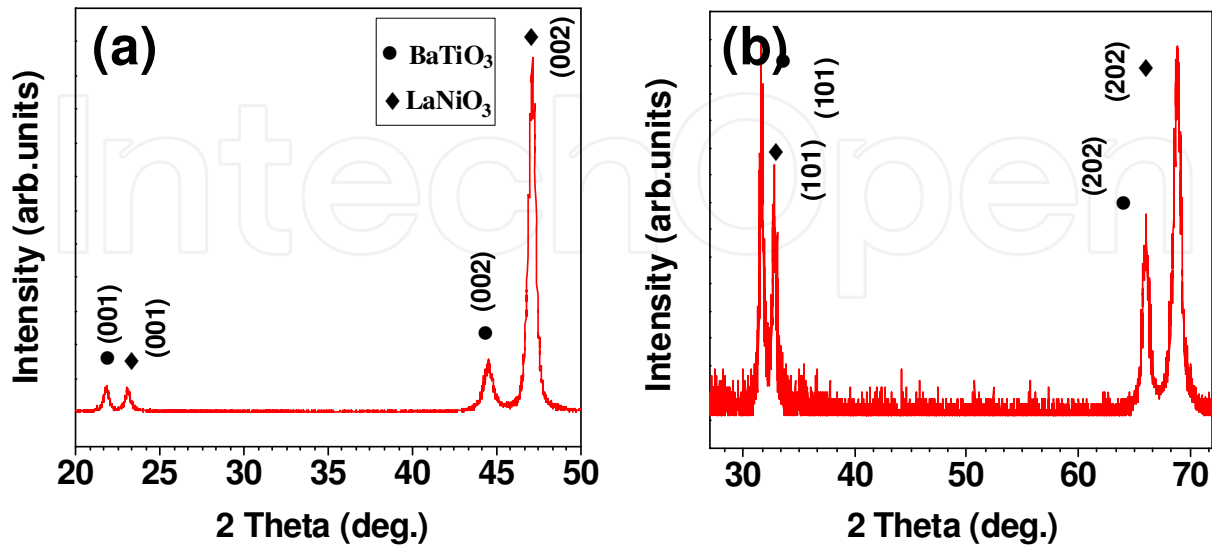

Fig. 14. XRD patterns of regular (a) and 45° tilted (b) θ-2θ scans of BTO(100nm)/LNO(600nm)/Si.
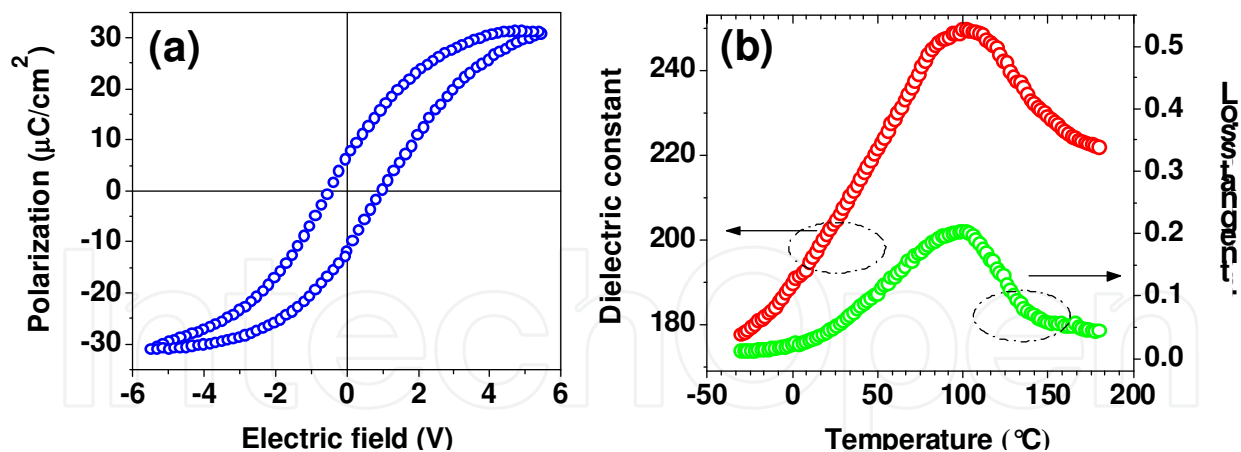
Fig. 15. Room temperature hysteresis loop (a) and temperature dependent dielectric response (b) for compressive strained BTO film.

Electrical properties of compressive strained BTO film have been investigated by ferroelectric and dielectric measurements. Hysteresis loop for the compressive BTO, as shown in Fig. 15(a), exhibits a well-defined shape, which is significantly different from those of tensile BTO films. The P_r is 10.2 μC/cm² , much larger than 0.7 μC/cm² and 2.0 μC/cm² observed in tensile BTO films on Si substrate [41,44], which is apparently due to the compressive strain state induced by thick LNO layer. However, it should be noted that the obtained P_r is still smaller compared with the giant P_r values for other fully strained BTO films with purely c-domain structure on compressive oxide substrates, such as SrTiO$_3$ [46], GdScO$_3$ and DyScO$_3$ [47]. Temperature dependent dielectric permittivity and loss tangent curves exhibit a broad peak near 100 °C, showing a slight decrease in the ferroelectric to parelectric phase transition temperature (T_c) with respect to its bulk counterparts [75]. The strain state dependent T_c for BTO film had been extensively investigated, and it is very dependent on the film or buffer layer thickness [76,77], substrate chosen [78,79] as well as the microstructure and crystallinity [80,81] of the fabricated BTO films. For example, Huang et al. [76] had fabricated BTO films with wide range of thickness (35 ~ 1000 nm) on 400 nm LNO buffered Si substrates using Ar/O$_2$ mixed sputtering gas and found that all the films were tensile strained and the T_c was greatly reduced with decreasing the BTO film thickness. However, their BTO films were significantly (110)-oriented instead of (001)-oriented. On the other hand, based on the misfit strain-temperature phase diagrams theory for epitaxial polydomain ferroelectric thin films, both tensile and compressive epitaxial strain will substantially enhance the T_c for ideal homogeneous ferroelectric epitaxial films. However, it has recently been demonstrated that in thin films the inhomogeneous strain field resulted by the strain gradients in the growth direction of the film should also be considered, which, combined with the homogeneous strain field, will both influence the polarization and ferroelectric phase transition character of ferroelectric thin films [41,82,83]. In addition, Kato et al. [80] observed a marked decrease of T_c for 20 °C in polycrystalline BTO films on LNO(200nm)/Pt(400nm)/Si and Chen et al. [81] also reported a reduced T_c in polycrystalline multiferroic NiFe/BTO/Si.

In fact, the reduction of T_c for the ferroelectric crystals and films are commonly observed in a system under an external compressive stress [74,81]. Based on the soft mode theory, the phase transition for displacive ferroelectrics can be attributed to the frozen of soft mode in

Epitaxial Integration of Ferroelectric BaTiO₃ with Semiconductor Si:
From a Structure-Property Correlation Point of View
381

the center of Brillouin zone. The frequency of the soft mode (ω_T) is determined by the interaction between local restoring "short range" repulsions (R_0'), which prefers the undistorted paraelectric cubic structure, and "long range" Coulomb force, which stablizes the ferroelectric distortions [84],

$$\mu\omega_T^2 = R_0' - 4\pi(\varepsilon+2)(Z'e)^2/9V \qquad (9)$$

where, μ is the reduced mass of the ions, $Z'e$ the effective ionic charge, V the volume of the unit cell, and ε the high frequency dielectric constant. The decreased lattice volume in the compressive BTO film ($V_{film} < V_{teg} < V_{cubic}$) leads to the decrease of average ion distance (r), which in turn increases the short range force and the Coulomb force as well. Since the short range force is proportional to r^{-n} (n = 10~11) while the Coulomb force to r^{-3}, the increase of the former with decreasing r is much faster than the latter [85,86]. The result leads to the stiffening of the soft mode, resulting in a lower ferroelectric transition temperature from a macroscopic point of view.
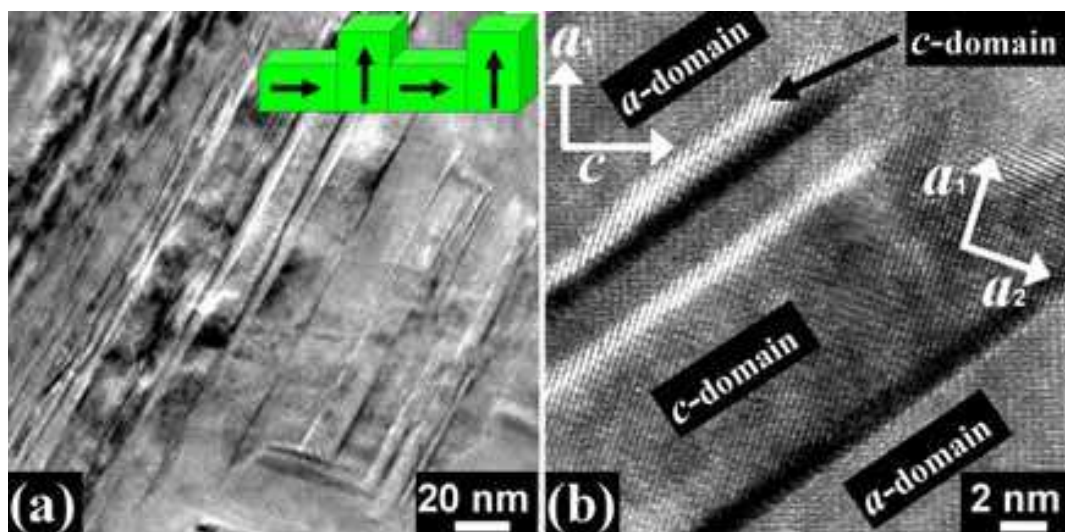

Fig. 16. (a) Plan-view TEM image of domain configurations and (b) HRTEM image of elastic domains for the compressive BTO film.

The compressive BTO exhibits very different domain configurations as compared with a tensile BTO, in which twining $a_1/a_2/a_1/a_2$ domain structure was observed. Fig. 16(*a*) shows plan-view TEM image of domains for the compressive BTO film, in which lamellar domain patterns are clearly observed. Further HRTEM observation, as shown in Fig. 16(*b*), reveals a $c/a/c/a$ domain pattern, in which c-domains have equal in-plane lattice parameters of $a_1=a_2$ with polarization vectors parallel to c-axis and a-domains have non-equal in-plane lattice parameters with polarization parallel to a-axis. These observations correspond well with the typical $c/a/c/a$ polydomain configurations in compressive ferroelectric films observed by Lee et al. [72] and Alpay et al. [87].

5.4 Phase transition
Fig. 17(a) shows the normal XRD pattern for a 300 nm BTO thin film grown on the 600nm LNO-buffered Si substrate. The lattice constants for BTO film are a = 3.982 and c = 4.053 Å, thus it can be inferred that the sputtered BTO film is under an in-plane compressive strain

state. Fig. 17(b) and (c) demonstrate the HRTEM images of typical ferroelectric domains for the BTO film. It is seen that a BTO grain is distinctively split by the appearance of laminar domain configurations in order to minimize the in-plane elastic strain energy [88]. Similarly, for this compressive strained BTO, the observed domain wall between adjacent domains exhibits a blunt fringe contrast, indicating a *c/a/c/a* domain configuration.
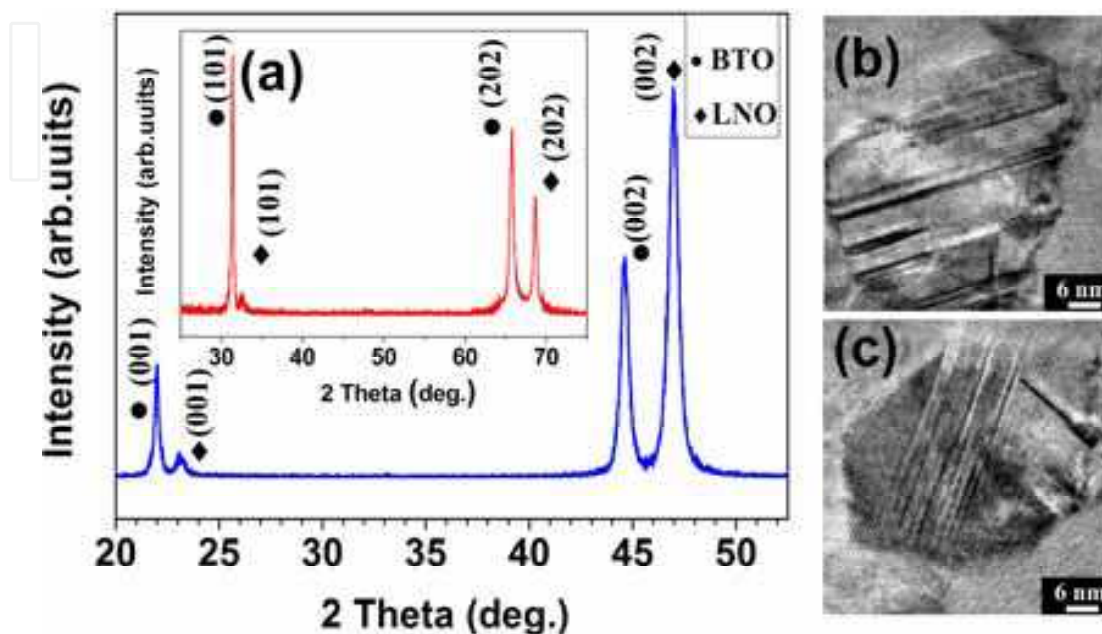

Fig. 17. (a) XRD θ - 2θ scan for 300 nm BTO on LNO(600nm)/Si. Inset is the 45° tilted XRD θ - 2θ scan for the same film. (b) and (c) HRTEM lattice image of typical ferroelectric domains inside a single BTO grain.

Fig. 18(a) and (b) show the temperature dependent dielectric constant (ε') and dielectric loss (tanδ) at different frequency of 1 - 500 kHz for the BTO film. It is observed that the Curie temperature (T_c), characterizing the ferroelectric to parelectric phase transition, is around 108 °C, which is lower than the value of typical T_c for BTO bulk or single crystal. On the other hand, in addition to the reduction of T_c, several other feathers are also evidenced in Fig. 18(a) and (b): (1) A broadened maximum in the dielectric constant appears at a wide temperature ranging from 80 °C to 120 °C, (b) the magnitude of the dielectric constant decreases, while T_c increases with increasing frequency, (c) the peak in dielectric loss is also frequency dependent and it shifts to higher temperatures with increasing frequency. The above observed strongly frequency dependent dielectric properties resemble the typical diffusive ferroelectric phase transition in ferroelectric relaxors rather than a normal ferroelectric phase transition, which shows a sharp anomaly at the T_c [89].

According to Smolensky and Uchino *et al*. [90,91], the diffuseness of the phase transition can be investigated by a modified Curie-Weiss (CW) law,

$$1/\varepsilon'-1/\varepsilon'_m= (T-T_m)^\gamma/C \qquad (10)$$

where ε' is the dielectric constant at temperature T, ε'_m is the dielectric constant at T_m, γ is the critical exponent, and C is the Curie constant. A value of $\gamma = 1$ indicates a normal transition with ideal CW behavior, whereas $\gamma = 2$ indicates a diffusive transition behavior. The plot of $\log(1/\varepsilon'-1/\varepsilon'_m)$ as a function of $\log(T-T_m)$ at 1 kHz is shown in the Fig. 19(a). By fitting the

Epitaxial Integration of Ferroelectric BaTiO$_3$ with Semiconductor Si:
From a Structure-Property Correlation Point of View
383

modified CW law, the exponent γ, determining the degree of the diffuseness of the phase transition, can be extracted from the slope of $\log(1/\varepsilon'-1/\varepsilon'_m)$ - $\log(T-T_m)$ plot. The relatively high γ value of 1.624 also indicates a relaxor behavior, which seems to be inconsistent with the predominant concept that BTO is a typical displacive ferroelectric material and should exhibit sharp dielectric transition [92].
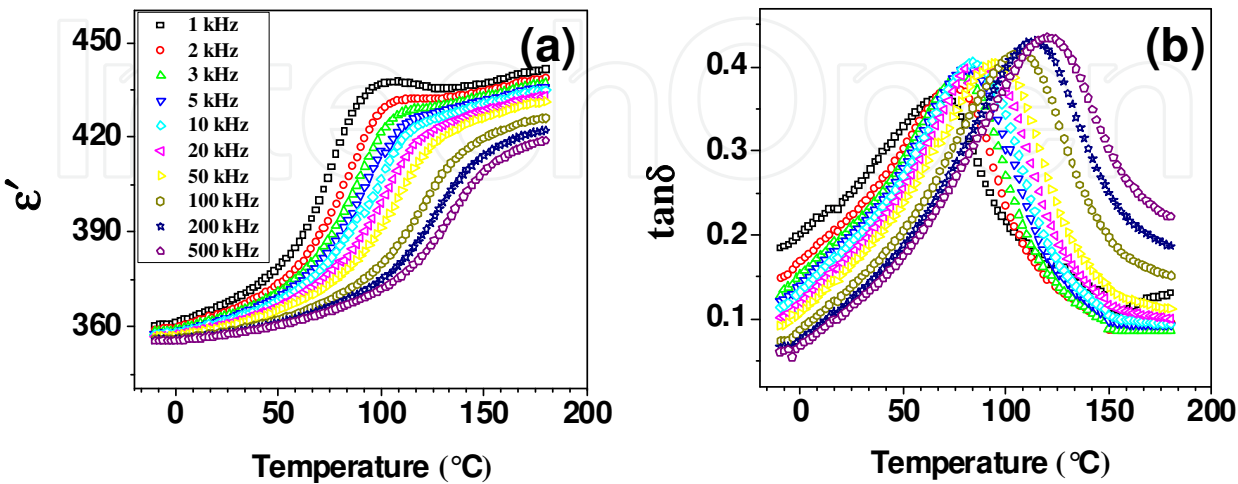
Fig. 18. Temperature dependent (a) dielectric constant and (b) loss tangent for the BTO film at frequency range of 1 kHz ~ 500 kHz.
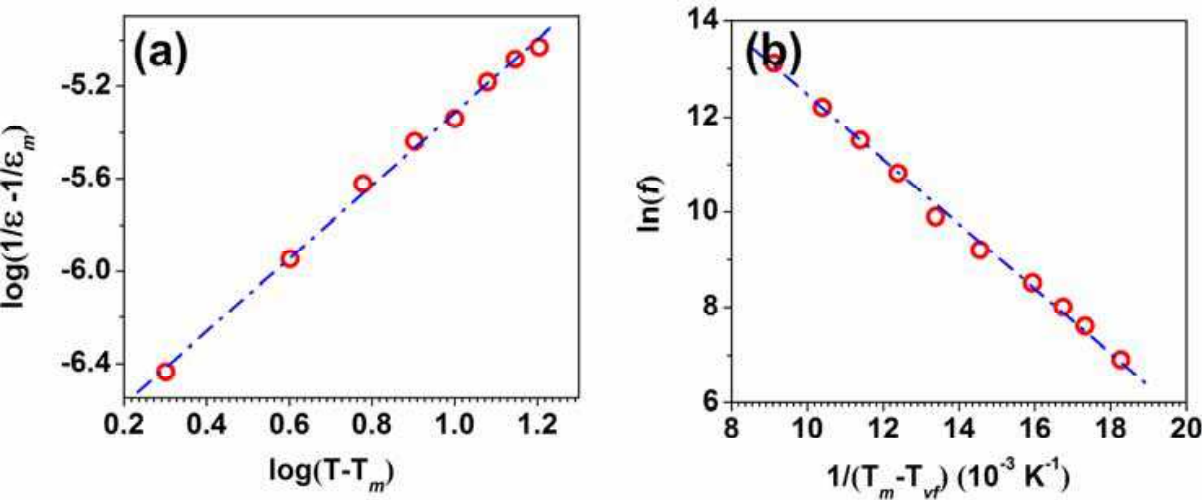

Fig. 19. (a) $\log(1/\varepsilon'-1/\varepsilon'_m)$ - $\log(T-T_m)$ plot for the BTO film at 1 kHz. (b) $\ln(f) - 1/(T_m-T_{vf})$ plot for the BTO film at 1 kHz. Symbol represents experimental data and solid dot line shows the fitting result.

However, recent nuclear magnetic resonance and Raman scattering studies had both evidenced the coexistence of the displacive character of transverse optical soft mode with the order-disorder character of Ti ions [93], especially in the BTO thin films. As the sputtering is proceed in an oxygen deficient atmosphere, thus the oxygen vacancies induced structural disorders and compositional fluctuations in the film may be responsible for the observed relaxor behavior. Similar diffusive transition had also been observed in BTO films on MgO and Pt-coated Si substrates [94,95].

The relaxor nature of the frequency dependent dielectric response of BTO film can also be examined by the Vogel-Fulcher (VF) relation [96],

$$f = f_0 \exp[-E_a / k(T_m - T_{vf})] \tag{11}$$

where f is the measuring frequency, f_0 is the characteristic relaxation frequency, E_a is the activation energy, T_m is the phase transition temperature at f, and T_{vf} is the freezing temperature of polarization-fluctuation. The $\ln(f) - 1/(T_m - T_{vf})$ plot with best fittings for the film is displayed in Fig. 19(b). The validity of VF relationship further demonstrates the relaxor behavior. From the slop of the fittings, the corresponding parameters can be obtained, $f_0 \sim 3.12108$ Hz, $T_{vf} \sim 327.3$ K and $E_a \sim 0.097$ eV.

6. Conclusions

High quality ferroelectric BTO thin films with (100)-preferred orientation have been grown on LNO buffered Si substrate by rf sputtering and the corresponding structure-property correlations have been discussed. Using combination of XRD and HRTEM, it is revealed that highly-oriented BTO film could be achieved on the lattice-mismatched Si in a "cube-on-cube" fashion with LNO as both buffer layer and conductive electrode layer. Polarization-switching measurement points out that while obvious ferroelectricity is obtained for BTO films with grain size larger than 22 nm, a weak ferroelectricity is still observed in BTO film of 14 nm grains, indicating that if a critical grain size exists for ferroelectricity it is less than 14 nm for BTO/LNO/Si system. We also demonstrate that due to their unique feature of gradient lattice constant and thermal expansion coefficient values for ferroelectric BTO, conductive LNO, and substrate Si, the BTO/LNO/Si system exhibits very interesting strain states. By choosing appropriate thicknesses for BTO and LNO, strain in ferroelectric BTO layer could be evolved from tensile strain to compressive strain state. The internal strain has a significant influence on the polarization, dielectric phase transition, and domain configuration for BTO film on Si and this can be used as a tool to engineer the properties of BTO films. The present work may have important implications on the future ferroelectric semiconductor devices.

7. Acknowledgements

8. References

[1] Y. Yano, K. Iijima, Y. Daitoh, a T. Terashim, Y. Bando, Y. Watanabe, H. Kasatani and H. Terauchi, *J. Appl. Phys.* 76, 7833 (1994).
[2] S. Kim and S. Hishita, *Thin Solid Films* 281-282, 449 (1996).
[3] L. Qiao and X. F. Bi, *Thin Solid Films* 517, 3784 (2009).
[4] R. E. Avila, J. V. Caballero, V. M. Fuenzalida and I. Eisele, *Thin Solid Films* 348 44 (1999).
[5] T. Pencheva and M. Nenkov, *Vacuum* 48, 43 (1997).
[6] D. Y. Kim, S. G. Lee, Y. K. Park and S. J. Park, *Mater. Lett.* 40, 146 (1999).

[7] X. H. Wei, Y. R. Li, J. Zhu, Z. Liang, Y. Zhang, W. Huang and S. W. Jiang, *Appl. Surf. Sci.* 252, 1442 (2005).

[8] T. W. Kim, M. Jung, Y. S. Yoon, W. N. Kang, H. S. Shin, S. S. Yom and J. Y. Lee, 1993 *Solid State Commun.* 86, 565 (1993).

[9] K. Yao and W. G. Zhu, *Thin Solid Films* 408, 11 (2002).

[10] W. Xu, L. Zheng, H. Xin, C. Lin and O. Masanori, *J. Electrochem. Soc.* 143, 1133 (1996).

[11] S. A. Chambers, *Adv. Mater.* 22, 219 (2010).

[12] J. W. Reiner, A. M. Kolpak, Y. Segal, K. F. Garrity, S. I. Beigi, C. A. Ahn, and F. J. Walker, *Adv. Mater.* 22, 2929 (2010).

[13] M. P. Warusawithana, C. Cen, C. R. Sleasman, J. C. Woicik, Y. L. Li, L. F. Kourkoutis, J. A. Klug, H. Li, P. Ryan, L. P. Wang, M. Bedzyk, D. A. Muller, L. Q. Chen, J. Levy, and D. G. Schlom, *Science* 324, 367 (2009).

[14] J. Schwarzkopf and R. Fornari, *Prog. Crystal Growth Character. Mater.* 52, 159 (2006).

[15] A. K. Tagantsev, N. A. Pertsev, P. Muralt, and N. Setter, *Phys. Rev. B* 65, 012104 (2001).

[16] W. Y. Park, K. H. Ahn, and C. S. Hwanga. *Appl. Phys. Lett.* 83, 4387 (2003).

[17] S. B. Mi, C. L. Jia, T. Heeg, O. Trithaveesak, J. Schubert, and K. Urban, J. Cryst. Growth 283, 425 (2005).

[18] O. Auciello, J. F. Scott, and R. Ramesh, Phys. Today 51(7), 22 1998).

[19] J. Levy, Phys. Rev. A 64, 052306 (2001).

[20] V. Vaithyanathan, J. Lettieri, W. Tian, A. Sharan, A. Vasudevarao, Y. L. Li, A. Kochhar, H. Ma, J. Levy, P. Zschack, J. C. Woicik, L. Q. Chen, V. Gopalan, and D. G. Schlom, J. Appl. Phys. 100, 024108 (2006).

[21] Y. S. Touloukian, R. K. Kirby, R. E. Taylor, and T. Y. R. Lee, Thermal Expansion, Nonmetallic Solids, Thermophysical Properties of Matter (Plenum, New York, 1977), Vol. 13.

[22] L. Qiao and X. F. Bi, J. Cryst. Growth 310, 5327 (2008).

[23] L. W. Martin, Y. H. Chu, R. Ramesh, *Mater. Sci. Eng. Rep.* 68, 111 (2010).

[24] A. B. Posadas, M. Lippmaa, F. J. Walker, M. Dawber, C. H. Ahn, and J. M. Triscone, *Topics. Appl. Phys.* 105, 219 (2007).

[25] E. Kawamura, V. Vahedi, M. A. Lieberman, and C. K. Birdsall, *Plasma Sources Sci Technol* R45, 240 (1999).

[26] B. G. Chae, Y. S. Yang, S. H. Lee, M. S. Jang, S. J. Lee, S. H. Kim, W. S. Baek, S. C. Kwon, *Thin Solid Films* 410, 107 (2002).

[27] N. Wakiya, T. Azuma, K. Shinozaki, N. Mizutani, *Thin Solid Films* 410, 114 (2002).

[28] D. H. Bao, N. Mizutani, X. Yao and L. Y. Zhang, *Appl. Phys. Lett.* 77, 1041 (2000).

[29] Q. Zou, H. E. Ruda and B. G. Yacobi, *Appl. Phys. Lett.* 78, 1282 (2001).

[30] D. H. Bao, N. Wakiya, K. Shinozaki, N. Mizutani and X. Yao, *Appl. Phys. Lett.* 78, 3286 (2001).

[31] J. R. Cheng, L. He, S. W. Yu and Z. Y. Meng, *Appl. Phys. Lett.* 88, 152906 (2006).

[32] S. Schlag and H. F. Eicke, *Solid State Commun.* 91, 883 (1994).

[33] W. Zhong, B. Jiang, P. Zhang, J. Ma, H. Chen, Z. Yang and L. Li, *J. Phys.: Condens. Matter* 5, 2619 (1993).

[34] S. Chattopanhuay, P. Ayyub, V. R. Palkar and M. Multani, *Phys. Rev. B* 52, 13177 (1995).

[35] S. Li, J. A. Eastman, J. M. Vetrone, C. M. Foster, R. E. Newnham and L. E. Cross, *Jpn. J. Appl. Phys., Part I* 36, 5169 (1997).

[36] T. Maruyama, M. Saitoh, I. Sakay and T. Hidaka, *Appl. Phys. Lett.* 73, 3524 (1998).

[37] Y. S. Kim, D. H. Kim, J. D. Kim, Y. J. Chang, T. W. Noh, J. H. Kong, K. Char, Y. D. Park, S. D. Bu, J.-G. Yoon and J.-S. Chung, *Appl. Phys. Lett.* 86, 102907 (2005).

[38] J. Junquera and P. Ghosez, *Nature* 422, 506 (2003).

[39] D. D. Fong, G. B. Stephenson, S. K. Streiffer, J. A. Eastman, O. Auciello, P. H. Fuoss and C. Thompson, *Science* 304, 1650 (2004).

[40] A. R. Meier, F. Niu and B. W. Wessels, *J. Crystal Growth*, 294, 401 (2006).

[41] B. Dkhil, E. Defay and J. Guillan, *Appl. Phys. Lett.* 90, 022908 (2007).

[42] H. Huang, X. Yao, M. Q. Wang and X. Q. Wu, *J. Crystal Growth* 263, 406 (2004).

[43] Y. P. Guo, K. Suzuki, K. Nishizawa, T. Miki and K. Kato, *J. Crystal Growth* 284, 190 (2005).

[44] R. Thomas, V. K. Varadan, S. Komarneni and D. C. Dube, *J. Appl. Phys.* 90, 1480 (2001).

[45] L. M. Huang, Z. Y. Chen, J. D. Wilson, S. Banerjee, R. D. Robinson, I. P. Herman, R. Laibowitz and S. O'Brien, *J. Appl. Phys.* 100, 034316 (2006).

[46] Y. S. Kim, J. Y. Jo, D. J. Kim, Y. J. Chang, J. H. Lee, T. W. Noh, T. K. Song, J.-G. Yoon, J.-S. Chung, S. I. Baik, Y.-W. Kim and C. U. Jung, *Appl. Phys. Lett.* 88, 072909 (2006).

[47] K. J. Choi, M. Biegalski, Y. L. Li, A. Sharan, J. Schubert, R. Uecker, P. Reiche, Y. B. Chen, X. Q. Pan, V. Gopalan, L. Q. Chen, D. G. Schlom and C. B. Eom, *Science* 306, 1005 (2004).

[48] M. T. Buscaglia, M. Viviani, V. Buscaglia, L. Mitoseriu, A. Testino, P. Nanni, Z. Zhao, M. Nygren, C. Harnagea, D. Piazza andi C. Galass, *Phys. Rev. B.* 73, 064114 (2006).

[49] X. Y. Deng, X. H. Wang, H. Wen, L. L. Chen, L. Chen and L. T. Li, *Appl. Phys. Lett.* 88, 252905 (2006).

[50] X. H. Wang, X. Y. Deng, H. Wen and L. T. Li, *Appl. Phys. Lett.* 89, 162902 (2006).

[51] G. Liu, X. H. Wang, Y. Lin, L. T. Li and C. W. Nan, *J. Appl. Phys.* 98, 044105 (2005).

[52] Y. Park and H-G. Kim, *J. Am. Ceram. Soc.* 80(1), 106 (1997).

[53] T. Takeuchi, M. Tabuchi, H. Kageyama and Y. Suyama, *J. Am. Ceram. Soc.* 82(4), 939 (1999).

[54] G. Arlt, D. Hennings and G. de With, *J. Appl. Phys.* 58, 1619 (1985).

[55] J. H. Haenl, P. Irvin, W. Chang, R. Uecker, P. Reiche, Y. L. Li, S. Choudhury, W. Tian, M. E. Hawley, B. craigo, A. K. Tagantsev, X. Q. Pan, S. K. Streiffer, L. Q. Chen, S. W. Kirchoefer, J. Levy, and D. G. Schlom, *Nature* 430, 758 (2004).

[56] J. Q. He, E. Vasco, R. Dittmann, and R. H. Wang, *Phys. Rev. B* 73, 125413 (2006).

[57] H. D. Kang, W. H. Song, S. H. Sohn, H. J. Jin, S. E. Lee, and Y. K. Chung, *Appl. Phys. Lett.* 88, 172905 (2006).

[58] M. Jimi, T. Ohnishi, K. Terai, M. Kawasaki, M. Lippmaa, *Thin Solid Films* 486, 158 (2005).

[59] N. A. Pertsev, A. G. Zembilgotov, S. Hoffmann, R. Waser, and A. K. Tagantsev, J. Appl. Phys. 85, 1698 (1999).

[60] K. S. Lee and S. Baik, J. Appl. Phys. 87, 8035 (2000).

[61] R. Dittmann, R. Plonka, E. Vasco, N. A. Pertsev, J. Q. He, C. L. Jia, S. Hoffmann, and R. Waser, Appl. Phys. Lett. 83, 5011 (2003).

[62] R. People and J. C. Bean, Appl. Phys. Lett. 47, 322 (1985).

Epitaxial Integration of Ferroelectric BaTiO$_3$ with Semiconductor Si:
From a Structure-Property Correlation Point of View
387

[63] J. M. Gere and S. P. Timoshenko, *Mechanics of Materials*, 4th ed. (PWS, Boston, 1997), p. 889.

[64] M. S. Rafique and N. Tahir, *Vacuum* 81, 1062 (2007).

[65] D. Y. Wang, Y. Wang, X. Y. Zhou, H. L. W. Chan and C. L. Choy, *Appl. Phys. Lett.* 86, 212904 (2005).

[66] N. A. Pertsev, V. G. Koukhar, R. Waser, and S. Hoffmann, *Integrated Ferroelectrics* 32, 235 (2001)

[67] N. A. Pertsev, A. G. Zembilgotov and A. K. Tagantsev, *Phys. Rev. Lett.* 80, 1988 (1998).

[68] N. A. Pertsev, A. G. Zembilgotov and A. K. Tagantsev, *Ferroelectrics* 223, 79 (1999).

[69] N. A. Pertsev and V. G. Koukhar, *Phys. Rev. Lett.* 84, 3722 (2000).

[70] V. G. Koukhar, N. A. Pertsev, and R. Waser, *Phys. Rev. B* 64, 214103 (2001).

[71] Y. L. Li and L. Q. Chen, *Appl. Phys. Lett.* 88, 072905 (2006).

[72] K. S. Lee, J. H. Choi, J. Y. Lee, and S. Baik, *J. Appl. Phys.* 90, 4095 (2001).

[73] A. Petraru, N. A. Pertsev, H. Kohlstedt, U. Poppe, R. Waser, A. Solbach, and U. Klemradt, J. Appl. Phys. 101, 114106 (2007).

[74] Z. H. Dai, Z. Xu, and X. Yao, Appl. Phys. Lett. 92, 072904 (2008).

[75] D. A. Tenne, X. X. Xi, Y. L. Li, L. Q. Chen, A. Soukiassian, M. H. Zhu, A. R. James, J. Lettieri, D. G. Schlom, W. Tian and X. Q. Pan, *Phys. Rev. B* 69, 174101 (2004)

[76] G. F. Huang and S. Berger, *J. Appl. Phys.* 93, 2855 (2003).

[77] L. Qiao and X. F. Bi, *J. Phys. D: Appl. Phys.* 41, 195407 (2008).

[78] K. M. Ring and K. L. Kavanagh, *J. Appl. Phys.* 94, 5982 (2003).

[79] M. E. Marssi, F. L. Marrec, I. A. Lukyanchuk and M. G. Karkut, *J. Appl. Phys.* 94, 3307 (2003).

[80] K. Kato, K. Tanaka, K. Suzuki and S. Kayukawa, *Appl. Phys. Lett.* 91, 172907 (2007).

[81] Y. C. Chen, T. H. Hong, Z. X. Jiang and Q. R. Lin, *J. Appl. Phys.* 103, 07E305 (2008).

[82] G. Catalan, B. Noheda, J. McAneney, L. J. Sinnamon, and J. M. Gregg, Phys. Rev. B 72, 020102R (2005).

[83] G. Catalan, L. J. Sinnamon, and J. M. Gregg, J. Phys.: Condens. Matter 16, 2253 (2004).

[84] W. Cochran, Phys. Rev. Lett. 3, 412 (1959).

[85] G. A. Samara, T. Sakudo, and K. Yoshimitsu, Phys. Rev. Lett. 35, 1767 (1975)

[86] R. E. Cohen, Nature 358, 136 (1992).

[87] S. P. Alpay, V. Nagarajan, L. A. Bendersky, M. D. Vaudin, S. Aggarwal, R. Ramesh, and A. L. Roytburd, *J. Appl. Phys.* 85, 3271 (1999).

[88] I. T. Kim, J. W. Jang, H. J. Youn, C. H. Kim and K. S. Hong, *Appl. Phys. Lett.* 72, 308 (1998).

[89] B. D. Qu, M. Evstigneev, D. J. Johnson and R. H. Prince, *Appl. Phys. Lett.* 72, 1394 (1998).

[90] G. A. Smolensky, *J. Phys. Soc. Jpn.* 28, 26 (1970).

[91] K. Uchino and S. Nomura, *Ferroelectr. Lett. Sect.* 44, 55 (1982).

[92] M. M. Kumar, K. Srinivas and S. V. Suryanarayana, *Appl. Phys. Lett.* 76, 1330 (2000).

[93] M. Tyunina and J. Levoska, *Phys. Rev. B* 70, 132105 (2004).

[94] S. Chattopadhyay, A. R. Teren, J. H. Hwang, T. O. Mason and B. W. Wessels, J. Mater. Res. 17, 669 (2002).

[95] R. Thimas, V. K. Varadan, S. Komarneni and D. C. Dube, *J. Appl. Phys.* 90, 1480 (2001).

[96] J. Xu and Y. Akishige, *Appl. Phys. Lett.* 92, 052902 (2008).
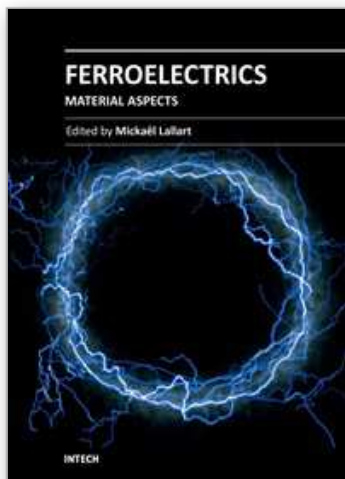
Ferroelectrics - Material Aspects

Edited by Dr. Mickaël Lallart

Ferroelectric materials have been and still are widely used in many applications, that have moved from sonar towards breakthrough technologies such as memories or optical devices. This book is a part of a four volume collection (covering material aspects, physical effects, characterization and modeling, and applications) and focuses on ways to obtain high-quality materials exhibiting large ferroelectric activity. The book covers the aspect of material synthesis and growth, doping and composites, lead-free devices, and thin film synthesis. The aim of this book is to provide an up-to-date review of recent scientific findings and recent advances in the field of ferroelectric materials, allowing a deep understanding of the material aspects of ferroelectricity.

How to reference

In order to correctly reference this scholarly work, feel free to copy and paste the following:

Liang Qiao and Xiaofang Bi (2011). Epitaxial Integration of Ferroelectric BaTiO3 with Semiconductor Si: From a Structure- Property Correlation Point of View, Ferroelectrics - Material Aspects, Dr. Mickaël Lallart (Ed.), ISBN: 978-953-307-332-3, InTech, Available from: http://www.intechopen.com/books/ferroelectrics-material-aspects/epitaxial-integration-of-ferroelectric-batio3-with-semiconductor-si-from-a-structure-property-correl

INTECH
open science | open minds